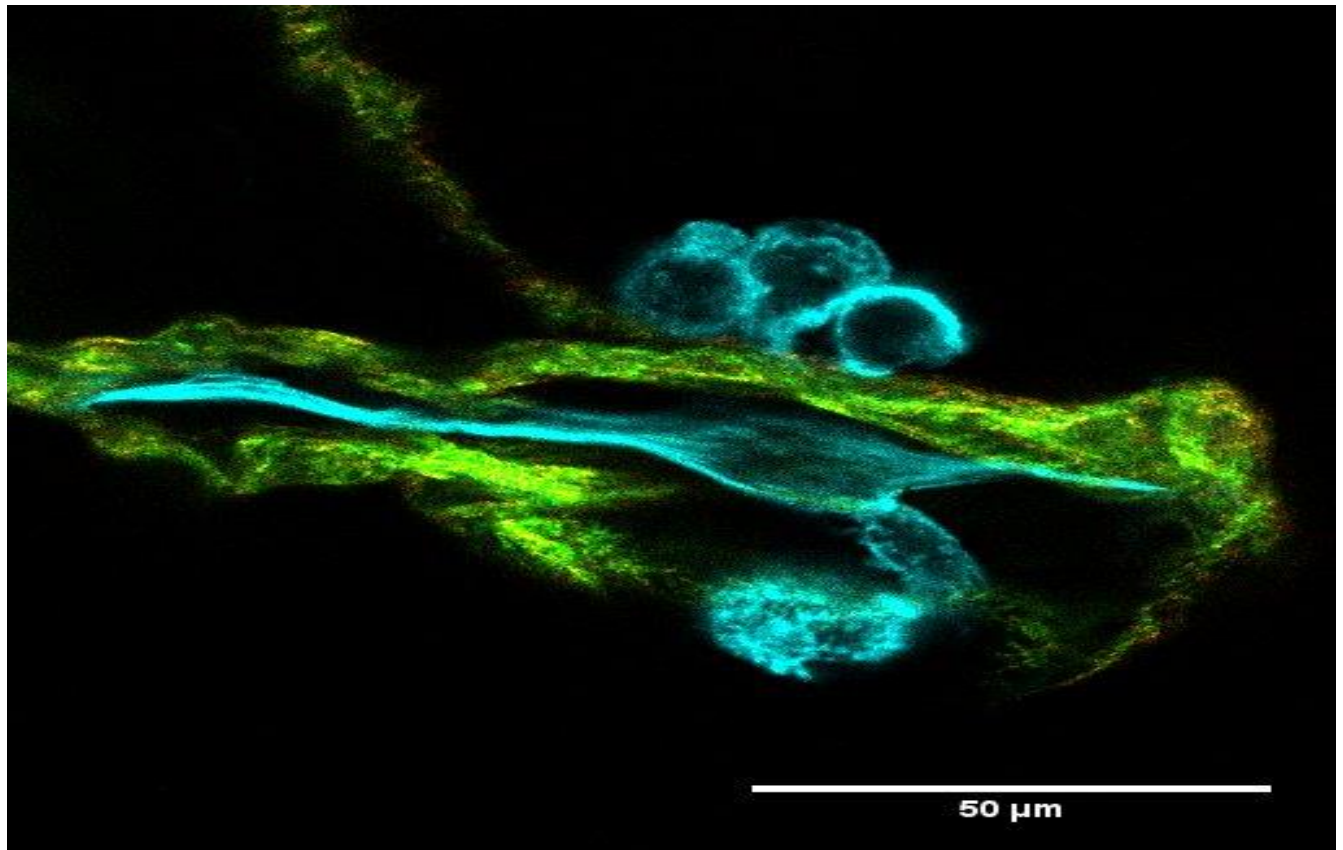




CHALMERS
UNIVERSITY OF TECHNOLOGY



Engineering of Micro-Patterned Protein Scaffolds for the Study of Cancer Cell Behavior

Master's thesis in Biomedical Engineering

Arsalan Latif

Department of Biology and Biological Engineering
CHALMERS UNIVERSITY OF TECHNOLOGY
Gothenburg, Sweden 2016

MASTER'S THESIS

Engineering of Micro-Patterned Protein Scaffolds for the Study of Cancer Cell Behavior

Master's Thesis within Biomedical Engineering

ARSALAN LATIF

SUPERVISORS

Alexandra Paul

Chalmers University of Technology, Gothenburg

Stéphanie Blockhuys

Chalmers University of Technology, Gothenburg

EXAMINER

Annika Enejder

Chalmers University of Technology, Gothenburg

Department of Biology and Biological engineering
CHALMERS UNIVERSITY OF TECHNOLOGY
Gothenburg, Sweden 2016

Engineering Micro-Patterned Protein Scaffolds for the Study of Cancer Cell Behavior

Master's Thesis within the Biomedical Engineering Master's Program

ARSALAN LATIF

© ARSALAN LATIF 2016.

Department of Biology and Biological engineering
Chalmers University of Technology
SE-412 96 Gothenburg
Sweden
Telephone + 46 (0)31-772 10 00

Cover:

Breast cancer cells within the porous Collagen-HA scaffold (developed at a freezing temperature of -55°C). Collagen type I in green and red (SHG), F-actin stained cells in cyan (MPEF).

Printed at Chalmers Reproservice
Gothenburg, Sweden 2016

Abstract

Cancer is a leading cause of death in the developed world, where up to 90% of cancer related deaths are due to metastasis. Breast cancer accounts for 25% of all cancer related deaths. During metastasis, the cancer cells infiltrate tissues and blood vessels by migration. A better understanding of what drives cancer cells to migrate and how they could be stopped is needed in order to develop more effective drugs that prevent metastasis. It is known that cancer cell behavior is regulated by both physical and chemical external stimuli, and their behavior in two-dimensional (2D) environments is vastly different from three-dimensional (3D) surroundings. Both 2D and 3D surfaces are found *in vivo*, therefore it is important to evaluate the cell behavior in both 2D and 3D *in vitro* surfaces. In this study, we assess the behavior of invasive breast cancer cells in a 2D and a 3D matrix by creating nanowrinkled surfaces on and pores in tissue mimicking protein hydrogels. Collagen type I – Hyaluronic Acid (HA) and elastin-like polypeptide (ELP) hydrogels were modified with well-controlled topographical traits. Both the tissue mimicking hydrogels and cancer cell behaviour in their presence were evaluated with non-linear microscopy (NLM) techniques, namely, multi-photon excitation fluorescence (MPEF, autofluorescence and fluorescent stains), coherent anti-Stokes Raman scattering (CARS, chemical contrast based on vibrations) and second harmonic generation (SHG, collagen fibres). The fluorescent stains and MPEF microscopy reveal that the cells adopted either rounded or elongated cell morphology in the porous collagen type I scaffolds, being dependent on the pore diameter. On the contrary, the breast cancer cells did not thrive in the porous ELP scaffolds, possibly the large pore diameter of the porous ELP scaffold did not support the cells to attach fast enough or adverse reaction to the *in situ* crosslinking. The cells on the ELP nanowrinkled scaffolds adopted elongated morphology and aligned themselves in parallel to the wrinkles. Further, live-cell studies were conducted to observe the effect of the topographical traits on the migration mode of the cells. The morphology of cancer cells on different topographical traits emphasizes the plasticity of cancer cells, and hints towards specific cell migration modes dependent on topographical features.

Contents

| | | |
|----------|---|----------|
| 1 | Introduction..... | 1 |
| 1.1 | Aim | 2 |
| 2 | Background | 2 |
| 2.1 | Metastatic Location: Lung Parenchyma..... | 2 |
| 2.2 | Modes of Cancer Cell Migration | 4 |
| 2.2.1 | The ECM Determinants | 5 |
| 2.3 | Microscopy Techniques | 6 |
| 2.3.1 | Multi Photon Excitation Fluorescence (MPEF) | 6 |
| 2.3.2 | Coherent Anti-Stokes Raman Scattering (CARS) | 7 |
| 2.3.3 | Second Harmonic Generation (SHG)..... | 7 |
| 3 | Materials and Methods..... | 8 |
| 3.1 | Materials | 8 |
| 3.1.1 | Porous ELP-RGD and Nanowrinkle Scaffolds..... | 8 |
| 3.1.2 | Porous Collagen-HA | 8 |
| 3.1.3 | Cell Line | 8 |
| 3.1.4 | Cell Culturing..... | 8 |
| 3.2 | Production of ELP | 9 |
| 3.2.1 | Culture and Expression | 9 |
| 3.2.2 | Purification | 9 |
| 3.3 | Nanowrinkle Scaffold | 10 |
| 3.4 | Porous Elastin-Like Polypeptide Scaffolds..... | 11 |
| 3.4.1 | <i>Optimizing the Ratio Between ELP-RGD to PMMA beads</i> | 12 |
| 3.5 | Porous Collagen type I Scaffolds | 15 |
| 3.5.1 | Porogen Leaching..... | 15 |
| 3.5.2 | Freeze-Drying..... | 15 |
| 3.6 | Scaffold Characterization..... | 16 |
| 3.6.1 | Pore Size..... | 16 |
| 3.6.2 | Aspect Ratio..... | 17 |
| 3.6.3 | Porosity | 17 |
| 3.7 | Cell Seeding Conditions..... | 18 |
| 3.7.1 | Cell Viability: Collagen Type I and ELP-RGD Coat..... | 18 |

| | | |
|-------|--|----|
| 3.7.2 | Cell Encapsulation: Collagen Type I and ELP-RGD | 18 |
| 3.7.3 | Porous Collagen I-HA Scaffold..... | 18 |
| 3.7.4 | Porous ELP-RGD Scaffold..... | 18 |
| 3.7.5 | Nanowrinkle ELP Scaffold..... | 19 |
| 3.8 | Multi-modal Nonlinear Microscopy | 19 |
| 3.8.1 | Imaging: Fluorescent Stains..... | 20 |
| 3.8.2 | Imaging: SHG and CARS | 20 |
| 4 | Results and Discussion..... | 21 |
| 4.1 | Scaffold Development | 21 |
| 4.1.1 | Porous Elastin-Like Polypeptide Scaffolds..... | 21 |
| 4.1.2 | Porous Collagen type I - HA Scaffolds..... | 25 |
| 4.1.3 | Nanowrinkle ELP Scaffold..... | 29 |
| 4.2 | Cell Studies | 30 |
| 4.2.1 | Cell Viability on 2D Substrates: Collagen Type I and ELP-RGD..... | 30 |
| 4.2.2 | Cell Viability in 3D Substrates: Collagen Type I and ELP-RGD Encapsulation | 31 |
| 4.2.3 | Porous and Nanowrinkle Scaffolds | 33 |
| 5 | Conclusion and Future Outlook | 42 |
| 6 | Acknowledgements | 43 |

1 Introduction

According to a report published by the American Cancer Society, there were 14.1 million new cancer cases registered and 8.2 million cancer-related deaths reported worldwide in 2012. The leading cause of cancer death among women was linked to breast cancer, accounting for 25% of all cancer cases and taking up 15% of all cancer deaths among women [1]. The time course of breast cancer is long, taking between 5 and 30 years to develop. In order to study the development and behavior of breast cancer *in situ*, it takes in excess of 10-15 years [2]. Conducting such studies, although essential, is not feasible or reproducible. Disease models developed *in vitro*, on the other hand, offer the ability to study, control chemical and physical characteristics of diseased cell phenotypes. Additionally, *in vitro* models single-out chemical and physical factors that effect diseased cell phenotypes. There exists a need to develop appropriate and functioning *in vitro* models of breast cancer microenvironments.

Cancer has been described as complex ‘rogue’ organs, to which other cells are recruited and can be corrupted by the transformed cells. Cancer can be described not only as a disease of uncontrolled cell growth but also of uncontrolled cell migration. Breast cancer cells are known to metastasize to the brain, the bone, liver and the lungs; where they form secondary tumor sites, figure 1.

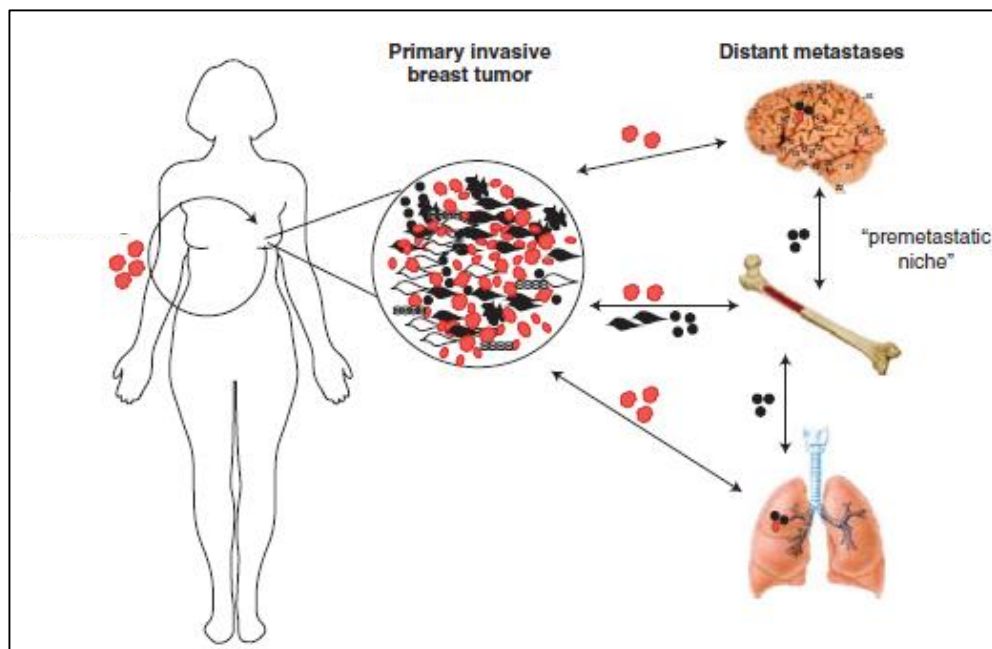


Figure 1: Cancer cells metastasize by entering the blood circulation and migrate to distant organs such as the brain, bone or the lungs to form secondary tumor sites (Figure taken from Polyak & Kalluri, 2010)

It has been understood that secondary metastatic tumor sites are the leading cause of death among cancer patients [3]. Thus it is not only important to mimic the original but also the secondary tumor

microenvironment in *in vitro* models. This project emphasizes on the development of the secondary tumor microenvironment in the parenchymal lung tissue.

1.1 Aim

The aim of the project is to study the behavior of MDA-MB-231 cells, a highly invasive breast cancer cell line, in a tissue engineered *in vitro* lung parenchymal environment.

2 Background

2.1 Metastatic Location: Lung Parenchyma

Primary breast cancer tumors are known to metastasize to the lung parenchyma, where they develop secondary tumor sites. The lung parenchyma consists of the elements of the respiratory system that are involved in gaseous transfer. This includes the alveoli, alveolar ducts and respiratory bronchioles, see figure 2. Studies have shown that parenchymal metastasis develop in the alveolar space[4], [5]. In this study we aim to recreate this complex situation *in vitro*.

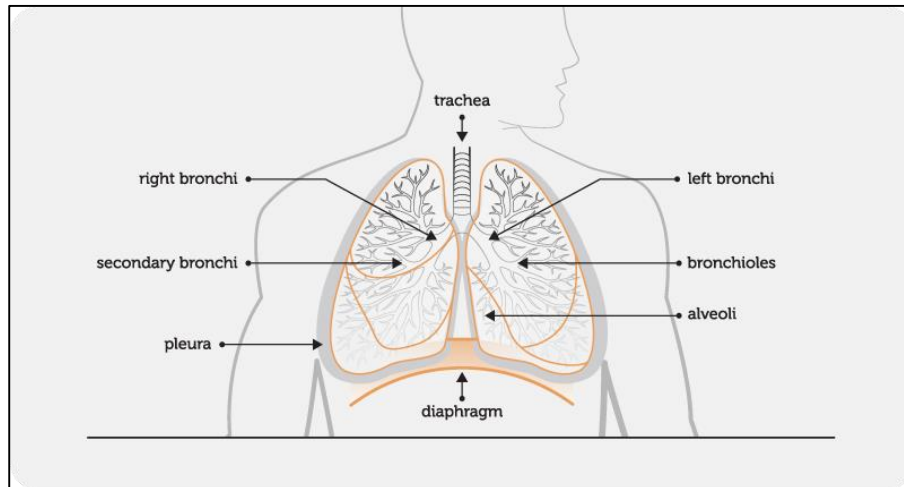


Figure 2: A schematic of the human respiratory system. The elements of the parenchyma include bronchioles and alveoli; which are involved in gaseous transfer. (Image taken from <http://bronchiectasis.com.au/bronchiectasis/bronchiectasis/definition>). Accessed: 01/09/2016)

The Extracellular Matrix (ECM) of the parenchyma is composed of collagen type I and III, elastin, laminin and glycosaminoglycan. Of which, collagen type I and III form the structural component of the alveolar space [6]. Structurally, the alveolar space is organized into highly porous, polygonal units with collagen type I and elastin walls, see figure 3. The collagen and elastin components form an interconnected pathway of pores between which cells can migrate. Further, the alveoli pore size has been found to be in the range of 150-250 μ m [4]

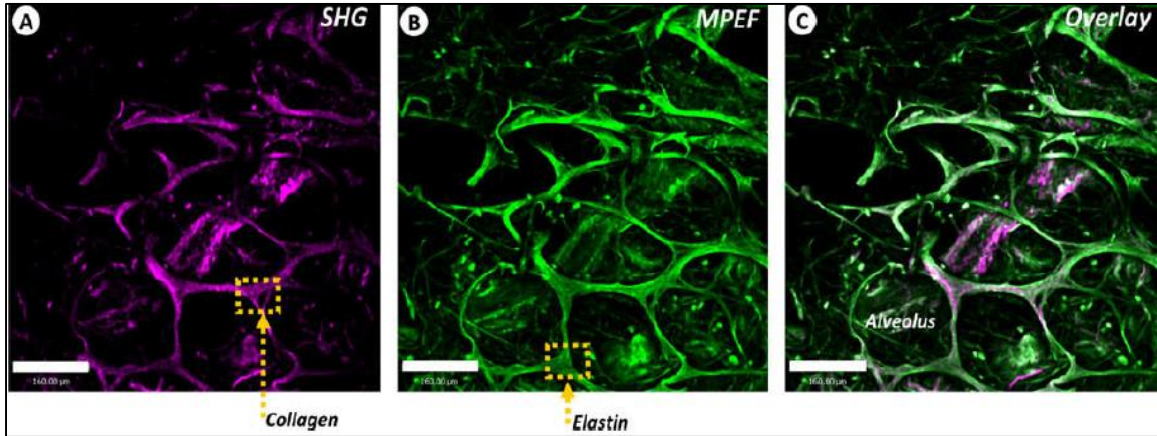


Figure 3: The highly porous alveolar space from a human lung. A) the second harmonic generation image from Collagen B) the fluorescence image from Elastin C) An overlay of both Collagen and Elastin. (Figure taken from Abraham & Hogg, 2010).

2.2 Modes of Cancer Cell Migration

Cancer cells have a unique ability to mold their migration patterns according to the environmental conditions experienced [7]. Cancer cells have two main methods of migration i) individual-cell migration and ii) collective cell migration, see figure 4 [8]. Both mechanisms involve engagement of cell surface receptors to the surrounding ECM. Single-cell migration consists of five

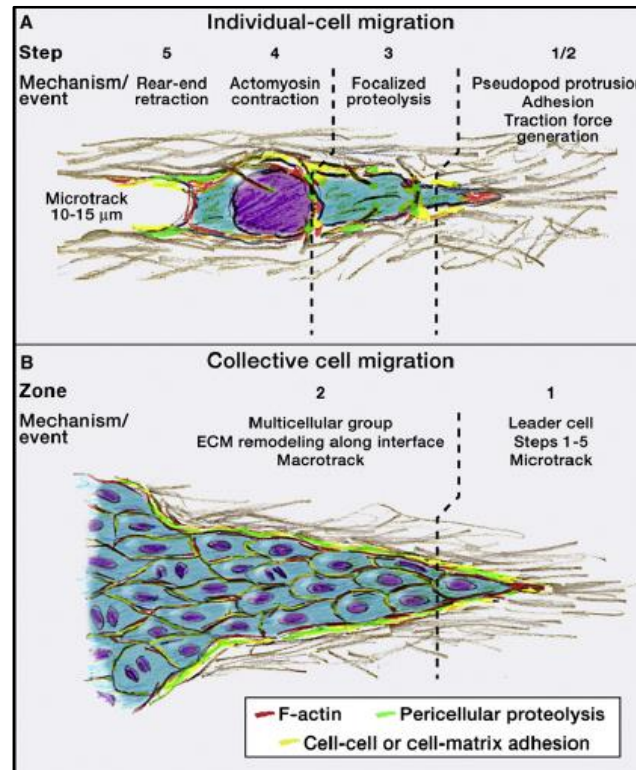


Figure 4: Cancer cells can either migrate as individuals (A) or as clusters (B). A) Individual-cell migration involves five molecular steps that elongate the cell and provide necessary traction force to propel it. B) The collective cell migration is divided into two zones: Zone 1, where the “leader” cell generates a microtrack and Zone 2, where following cells widen the track. (Figure taken from Friedl & Alexander, 2011).

interdependent steps that influence cell shape and position, figure 4A. In step 1, a leading edge is formed by actin polymerization. In step 2, the leading edge engages with the ECM, and the cell surface receptors form focal adhesion points. In step 3, the cell surfaces proteases behind the leading edge, release a controlled amount of protease. The ensuing proteolysis modifies the molecular and mechanical properties of the ECM; allowing the cell body to advance. Step 4 involves the contraction of the cell body through activation of actomyosin. The last step, step 5, involves the release of adhesion bonds at the trailing edge, which slides forward while the leading edge protrudes further. Collective cell migration involves the movement of cells in a supracellular manner [7], [9]. Where the group of cells behave as a mega-cell, figure 4B. This study focuses on single-cell migration, and therefore collective cell migration is not further discussed.

Single-cell migration can be further partitioned into i) rounded or amoeboid migration and ii) mesenchymal migration, see figure 5. These migration patterns involve little or no cell-cell junction. Amoeboid migration can then be further classified into: a) cells that rapidly change their morphology, have short thin protrusions b) cells with blebbing morphology and chaotic movements c) and cells with short cellular protrusions that are associated with proteolytic activity. The mesenchymal mode of migration is characterized by an elongated, spindle-like morphology of the cell body [9].


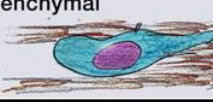
| | Cell-cell junctions | Tumor type |
|--|---------------------|--|
| Amoeboid  | - | Leukemia, lymphoma cell subsets (all tumors) |
| Mesenchymal  | - | Stromal tumors, epithelial tumors after EMT |

Figure 5: Single-cell migration can be divided into i) rounded or amoeboid migration ii) and mesenchymal migration. These single-cell migration patterns are known to be associated with tumor types (Figure adapted from Friedl & Alexander, 2011).

2.2.1 The ECM Determinants

Cell migration patterns are influenced by a number of variables, which include the cues received from the surrounding ECM. The ECM factors affecting cell migration have been studied *in vitro* and are outlined as follows: the ECM dimension, the density and pore size, the stiffness and the orientation [8].

2.2.1.1 ECM Dimension

In vivo the ECM architecture is either 2D or 3D and cellular migration can also happen in these different dimensions. Where, two-dimensional migration is commonly associated with re-epithelialization of wounds or scanning of leukocytes along inner blood vessel walls. In contrast, the migration of cells through interstitial tissue consisting of interwoven components of ECM constitutes migration of cells in three-dimension. The dimensionality of the ECM has a significant effect on the cell migration patterns. For 2D ECM, the cell will unilaterally attach to the substrate. It will adopt a flattened, spread-out cell morphology and will have mostly barrier free migration [10]. Such migration patterns are commonly noticed within inner epithelial surfaces [11]. In case of 3D ECM, the cells experience space limitations. These space limitations arise through the presence of interconnected ECM components in a 3D environment. The cells morphological change in a 3D environment is three fold; i) they adopt a spindle-like morphology ii) the leading edge protrusion forms cylindrical tip-like pseudopodia which orient in all three dimensions and iii) lastly, the cell distorts its shape to accommodate between small gaps or pores, and may even execute remodeling of the ECM [8].

2.2.1.2 ECM Density and Pore Size

The ECM significantly varies in its structural organization, which includes the ECM's texture and porosity. The porosity specifically has a fundamental effect on the migration efficiency of cells. Studies indicate that the ideal pore diameter for optimal migration efficiency is when the pore diameter matches or is slightly below the diameter of a polarized cell [12]. If the pore size exceeds the optimal then the migration rates decrease due to the lack of cell-substrate interaction. Further, the cells adopt amoeboid migration. While, if the pore size is below the cell diameter, then the migration rate decreases due to physical hindrance. In addition, the metastasizing cells elongate to form a spindle-like shape to migrate.

2.2.1.3 ECM Alignment

The connective tissue present *in vivo* consists either of highly aligned or random oriented ECM components. For instance, the ECM components on the invasive end of a tumor are highly aligned in order to facilitate metastasis. The presence of aligned ECM components modulates the cell morphology, and encourages multicellular streaming in 3D chainlike patterns or in 2D cell sheets [13].

2.3 Microscopy Techniques

2.3.1 Multi Photon Excitation Fluorescence (MPEF)

Conventional fluorescence microscopy involves excitation of the fluorophore, from the ground state to an electronic excited state, with a single photon. The return of the excited fluorophore to the electronic ground state results in an emitted photon, which is then captured by the detectors. The resulting emitted photon has lower energy than the excited photon; this is called the Stokes shift. This energy difference is associated with internal energy conversion of the fluorophore. The excitation process by a single photon can be substituted by simultaneous absorption of two or more

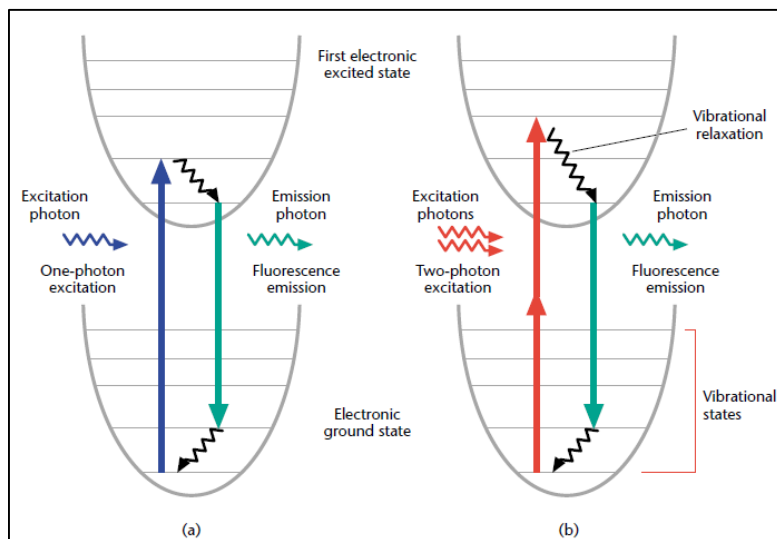


Figure 6: Energy diagram depicting the photon excitation and subsequent emission of fluorescence in A) single-photon excitation and b) two-photon excitation (Figure taken from So, 2002).

lower energy photons, see figure 6. The wavelength of the emitted photon is the same in both cases.

There are a number of advantages of MPEF over SPEF. First, the excitation wavelengths for MPEF are approximately twice of that of SPEF wavelengths. Thus, the wide separation between the excitation and emission spectra, allows efficient rejection of the excitation wavelength and Raman scattered photons, while detecting a maximum number of fluorescence photons. Second, MPEF microscopy has red excitation which penetrates deeper into the sample, and has lower scattering, and thus is optically suited for thick specimens. The near infra-red excitation beam has less absorption in biological tissues. Furthermore, the pulsed excitation beam in MPEF microscopy has maximum excitation power at the focus, making MPEF inherently confocal.

2.3.2 Coherent Anti-Stokes Raman Scattering (CARS)

Chemical bonds have characteristic vibrational frequencies, which are dependent on the composition of the molecule. Vibrational microscopy techniques, tap into these vibrational frequencies of different molecules. For instance, in Raman microscopy, the vibrational properties are measured as a change in frequency of an incident photon, termed Raman scattering. Essentially, the sample interacts with an incident photon, causing a) red shifting of the emitted photon, if the molecule absorbs energy from the photon b) blue shifting of the emitted light, if the photon absorbs energy from the molecule. The latter called anti-Stokes Raman scattering. Spontaneous Raman microscopy has a major limitation; the Raman effect is extremely weak, with photon conversion efficiency of less than 1 photon in 10^{18} photons [14], [15]. CARS overcomes this limitation, since the molecular vibrations are coherently driven by a wave mixing process between a pump beam (ω_p), probe beam (ω_{pr}) and the Stokes beam (ω_s). Where the wavelength of ω_p and ω_{pr} is typically the same. The difference between ω_p and ω_s constitutes the Raman active vibrational bond, which generates an anti-Stokes signal (ω_{as}) according to the following formula:

$$\omega_{as} = \omega_p + \omega_{pr} - \omega_s$$

The signal detected is stronger than the signal generated from Raman scattering. The technique permits visualization of unlabeled samples with high chemical specificity. CARS microscopy can be specifically used to visualize lipids and proteins, both of whom are commonly found in biological samples [14]. The limiting aspect of the microscopy technique is the non-resonant background, which makes quantitative image analysis challenging.

2.3.3 Second Harmonic Generation (SHG)

SHG is a resultant from light-matter interaction, where the matter enables a frequency doubling of an incident wave. This frequency doubling results in a reduction of emission wavelength by half. The SHG signal is in the order of the square of the incoming laser intensity, therefore the signal is mostly generated in the focus of the objective; where the power is highest. Quantum mechanical equations indicate that resonance only occur in non-centrosymmetric structures [16]. Collagen is inherently non-centrosymmetric and, thus SHG is widely used to image Collagen fibers [4], [17].

3 Materials and Methods

3.1 Materials

3.1.1 Porous ELP-RGD and Nanowrinkle Scaffolds

Reagents: ELP-RGD was produced in-house, and will be detailed in subsequent sections. The crosslinker, tetrakis hydroxymethyl phosphonium chloride (THPC) was purchased from Sigma-Aldrich. The solvent, tetrahydrofuran (THF) was obtained from VWR.

The topography causing traits; a) the PolyDimethylSiloxane (PDMS) molds were provided by Sarah Heilshorn's group, Stanford University b) and the Poly(methyl methacrylate) beads were bought from Cospheric.

3.1.2 Porous Collagen-HA

The Rat Tail Collagen type I (stock concentration 3.42mg/ml) was purchased from Merck Millipore. Both Sodium Hyaluronate or Hyaluronic Acid (HA) and N-(3-Dimethylaminopropyl)-N'-ethylcarbodiimide hydrochloride (EDC) were acquired from Sigma-Aldrich.

3.1.3 Cell Line

The epithelial breast cancer cell line, MDA-MB-231, was purchased from ATCC.

3.1.4 Cell Culturing

MDA-MB-231 cells were cultured in Dulbecco's Modified Eagles Medium (DMEM, Gibco) containing 10% Fetal Bovine Serum (FBS) and 1% Penicillin and Streptomycin (PEST, Fisher Scientific) in a T25 tissue culture-treated flask. Prior to seeding, confluent cells were detached with Tryple Express and counted with a Neubauer hemocytometer.

3.2 Production of ELP

A established protocol, provided by Sarah Heilshorn's biomaterials group at Stanford, was followed for the production of ELP from *Escherichia coli* (*E. coli*) bacteria [18]. The protocol involved multiple steps, summarized in figure 7.

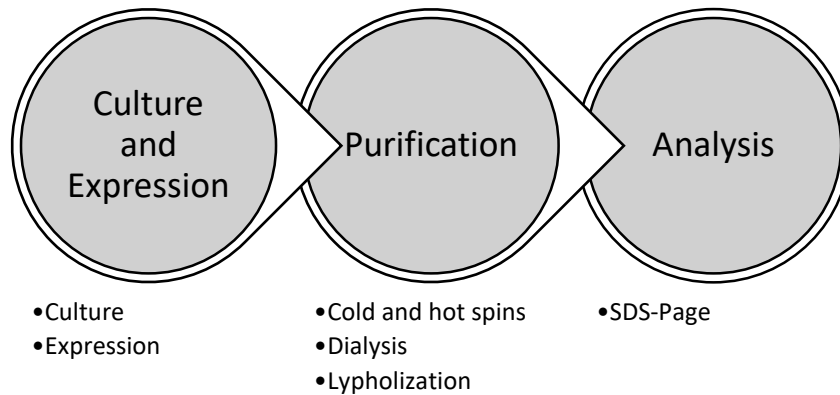


Figure 7: Schematic summarizing the steps involved in production of elp from e.coli

3.2.1 Culture and Expression

The ELP protein sequences were expressed in *E. coli* (BL21 DE3), and induced with 1M isopropyl β -D-1-thiogalactopyranoside (IPTG) at an OD600 of 0.8. Having induced protein expression, the cells are allowed to express for a period of 5-7 hours.

3.2.2 Purification

The cells are pelleted by centrifugation and lysed by three freeze-thaw cycles under the addition of DNase I and Phenylmethane sulfonyl fluoride (PMSF). A unique property of ELP is used to separate ELP from cell debris and other impurities. ELP possess a Lower Critical Solution Temperature (LCST), which means that below 4°C ELP is dissolved, while above 37°C it precipitates in aqueous solutions. Alternating cold and hot spins, i.e. centrifuging at 4°C or 37°C, permits the extraction of ELP using its inherit LCST. The ELP solution is then dialyzed with a 3.5kDa membrane to remove excess ions, after which the solution is lypholized to yield final product.

3.3 Nanowrinkle Scaffold

The nanowrinkled substrates were produced using ELP having either the RGD (ELP-RGD) or a hybrid scaffold with Hyaluronic Acid (HA). The wrinkles themselves are divided in two patterns based on their orientation; a) aligned (one-dimensional), or b) having an unaligned orientation, that is having no defined direction (two-dimensional). The wavelengths associated with both the 1D and 2D nanowrinkles is summarized in table 1.

Table 1: Two different sets of nanowrinkle orientation were used; 1D and 2D. The wavelengths associated with each of those orientations are listed.

| 1D | 2D |
|-------------|-------------|
| 1.6 μ m | 3.5 μ m |
| 3.5 μ m | Flat |
| Flat | |

Four components were needed to produce the nanowrinkled ELP: a) PDMS mold with specific orientation and wavelength of the nanowrinkles b) 12.5wt% ELP stock solution c) the crosslinker, THPC and d) round aminated cover slips with a diameter of 5 mm or 12 mm. The PDMS molds with the nanowrinkled pattern were provided by Teri Odom's group, Northwestern University. The 12.5wt% ELP stock solution in PBS was made in-house and stored at 4°C until use. The cover slips were aminated with 5% glacial acetic acid and 2% (3-aminopropyl) triethoxysilane for 1h at room temperature, followed by rinsing with ddH₂O and storage in ethanol until use.

To imprint the nanowrinkle pattern onto ELP; 10 μ l of the ELP, THPC mixture is pipetted onto the PDMS mold and the aminated cover slip is carefully placed on top. The THPC crosslinks the ELP, and crosslinks the aminated cover slip with the ELP. The stoichiometric crosslinking ratio between the hydroxyl group of THPC and primary amines of ELP were chosen to be 1:1 for all experiments. The crosslinking mechanism proceeded at 4°C for 1 hour followed by incubation at 37°C for 24 hours. The produced nanowrinkles are stored at 4°C until use.

3.4 Porous Elastin-Like Polypeptide Scaffolds

The protocol for developing porous ELP-RGD scaffolds was adapted from a protocol provided by Sarah Heilshorn's biomaterials group, Stanford University. Formation of porous ELP circulated around changing the ratio of ELP by volume to ratio of poly(methamethyl)acrylate (PMMA) beads by weight (V/W ratio). A set of varying ratios were tested. The porous gels were formed with the help of glass-bottom well-plates (Cellvis) and silicon isolator (ThermoFisher Scientific).

Two separate approaches with different addition techniques for the PMMA beads were implemented to produce porous ELP gels. The first approach involved use of silicon isolator within a 24-well plate. The silicon isolator has diameters of 6mm or 9 mm with a height of 0.5 mm, which theoretically should result in gels having an approximate volume of 28mm³ or 32 mm³, respectively. A single isolator was fitted into the 24-well plate into which the measured amount of PMMA beads were added. Having uniformly distributed the PMMA beads within the silicon isolator; the calculated amount of ELP can then be pipetted. The second approach does not make use of the 24-well plate. The silicon isolators are attached to coverslips into which the PMMA beads are added onto which the calculated amount of ELP is pipetted.

A number of different ratios were tried with approach 1; these ratios are listed in figure 8a. An initial ratio of 1:1 was used, after which the ratios were better optimized. Having noticed a fault in the first approach, the second approach involving use of the cover slip was then implemented. The ratios tested with the second approach are summarized in figure 8b.

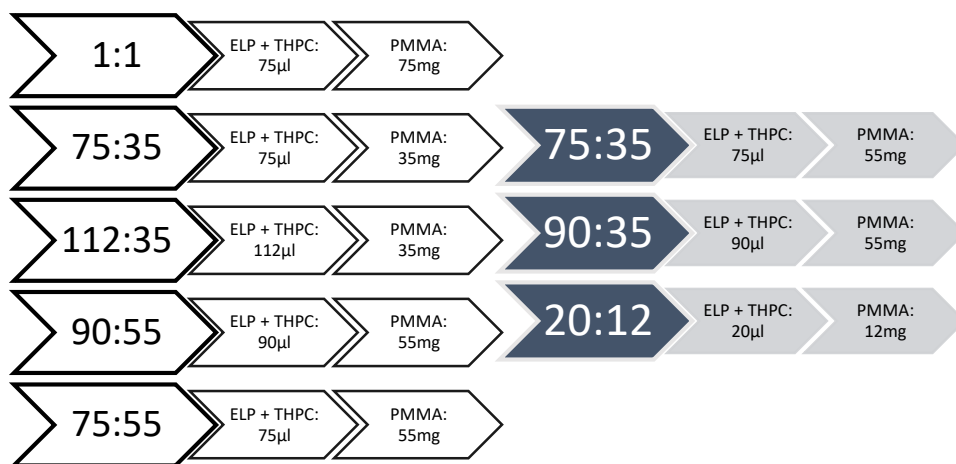


Figure 8: a) Summarizes ratios used for first approach b) summarized ratios used for second approach

In both approaches, after mixing the ELP and PMMA, the mixture is gelled with the addition of cross linker THPC with a ELP: THPC crosslinking ratio of 1:4. The resultant is then incubated at

37°C for 1 hour after which the silicon mold is removed and the gel placed within 25% THF overnight. It is then transferred into 100% THF for a period of 3 days. The THF solution is changed daily. The purpose of the THF is to dissolve the PMMA beads thereby creating a porous architecture within the gels. The complete removal of PMMA beads is checked through CARS microscopy.

3.4.1 *Optimizing the Ratio Between ELP-RGD to PMMA beads*

With a PMMA: ELP ratio of 1:1 the PMMA beads were not contained in the mold and additionally the ELP/PMMA mixture was too viscous and did not crosslink well. The second set of ratios made with the first approach were 75:35 and 112:35. Here it was also noted that the PMMA beads spilled to the edges of the well, however, most of the beads settled within the placeholder. The addition of ELP and THPC created a gel-like mixture. After an hour of incubation period the gels had cross-linked well and maintained its shape, see figure 9a. It was noted that the 112:35 gel had near to none porous structure indicating excessive ELP. While the 75:35 gel also exhibited far less porous structure it was more porous than 112:35, as shown in figure 9b.

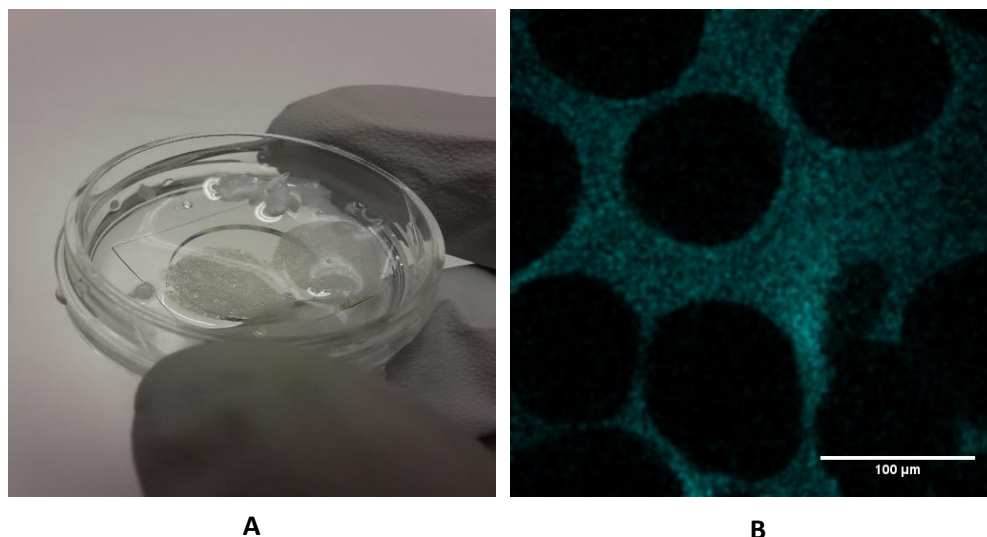


Figure 9: A) the 75:35 and 112:35 immersed in PBS B) Fluorescence image of the porous structure imaged in the 75:35 gel.

The gel ratios of 75:55 and 90:55 had more PMMA as compared to the second set of ratios. It was speculated that the increasing the amount of PMMA beads while having consistent ELP amounts would cause greater porosity and conserve the gel integrity. This proved to be true. The gels formed kept their structure, and had greater porosity, see figure 10.

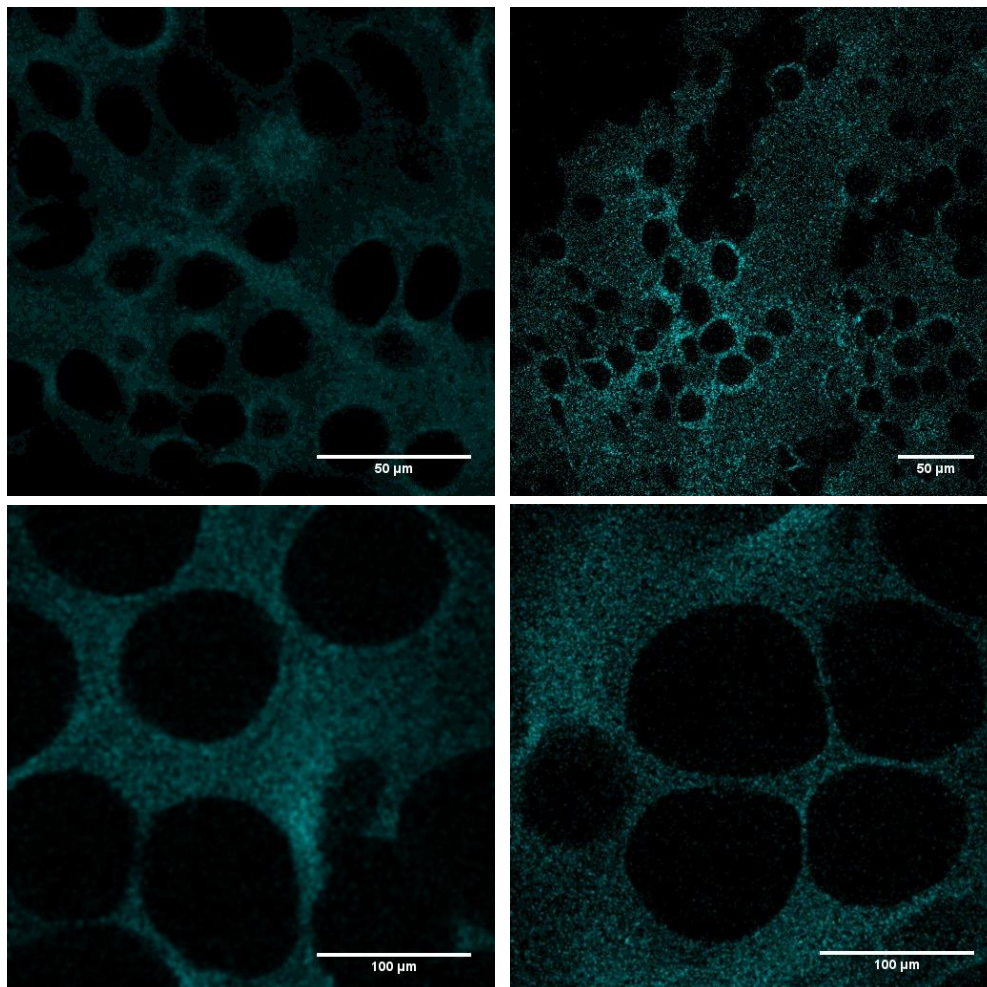


Figure 10: Top left and right, images of gel made of 90:55. pore sizes of 20-27 μ m. Bottom left and right, image of gel made from ratio 75:55. pore sizes of 106-125 μ m.

However, a similar, consistent phenomena was observed in producing all the gels with the first approach. Due to electrostatic attraction between the well walls and the PMMA beads, two hindrances arose; a) a great portion of the PMMA beads were spread around the placeholder instead of being within it b) the gels were partially or completely destroyed while being removed from within the well. This prompted the use of a cover slip instead of the well-plate in the second approach.

The ratios of 75:35 and 90:35 were repeated with the second approach. This was done to evaluate whether the change in approach had an effect on the integrity and porosity of the gel. The gels retained the dimensions of silicon mold. However, it was noted that the gels had a transparent appearance; which possibly pointed towards lack of ELP. A lack of ELP compromises the structural integrity of the gel. The second approach had two benefits; foremost the PMMA beads can be carefully added, ensuring that the beads remain within the confines of the placeholder. Secondly, the formed gel is easily removed from the placeholder and retains its integrity.

It was noted that both ELP and the PMMA beads could be conserved if the volume of the disc-shaped silicon placeholder could be calculated. The used silicon mold had a diameter of 9mm and height of 0.5mm; which brought the volume contained within the mold to be 31.8mm^3 or approximately $31.8\mu\text{l}$. Keeping this in mind, a ratio of 16:11 was used. The resulting gel was too thin and was destroyed while retrieving it from the silicon placeholder. Based on the fore mentioned results, the following changes were made: a) silicon placeholder with diameter 6mm and height 1mm (volume 28.3mm^3) used b) A ratio of 20:12 implemented. This combination resulted in a disc shaped gel with geometry of the silicon placeholder. Further, imaging revealed that an abundance of pores were present, figure 11.

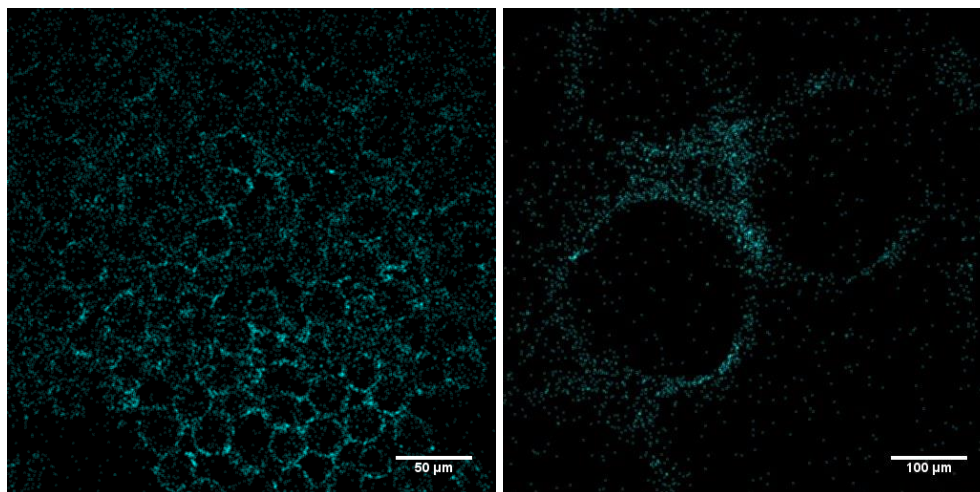


Figure 11: The pore density for 20:12 was adequate. Two different pore sizes of the same ratio were imaged. In both cases densely populated pores were formed. Left: $20\mu\text{m}$ - $27\mu\text{m}$. Right: $250\mu\text{m}$ - $300\mu\text{m}$.

In conclusion, the following ratios were earmarked as possible candidates; 75:55, 90:55 and 20:12. The second approach proved to be able to produce integral, reproducible gels, which caused minimal loss of resources, and so, this was chosen as the approach to be followed. Not a vast difference was noticed between the 75:55 and 90:55 gels; however, the 20:12 utilizes a lower amount of resources as compared to 75:55 and 90:55. The 20:12 gels, on the other hand, formed gels with thickness less than 0.5mm. The thin nature of the gels would not offer enough pore layers

to be considered a 3D environment. The 90:55 gels were bookmarked for cell seeding and scaffold characterization.

3.5 Porous Collagen type I Scaffolds

A number of techniques were exploited to develop porous Col -1 scaffolds. The techniques differ in their manner of introducing porogens [19], [20]. Based on the porogen introduction, the development methods are divided into porogen leaching and freeze-drying, which are further subdivided into type of porogen or chemical crosslinker used, summarized in figure 12.

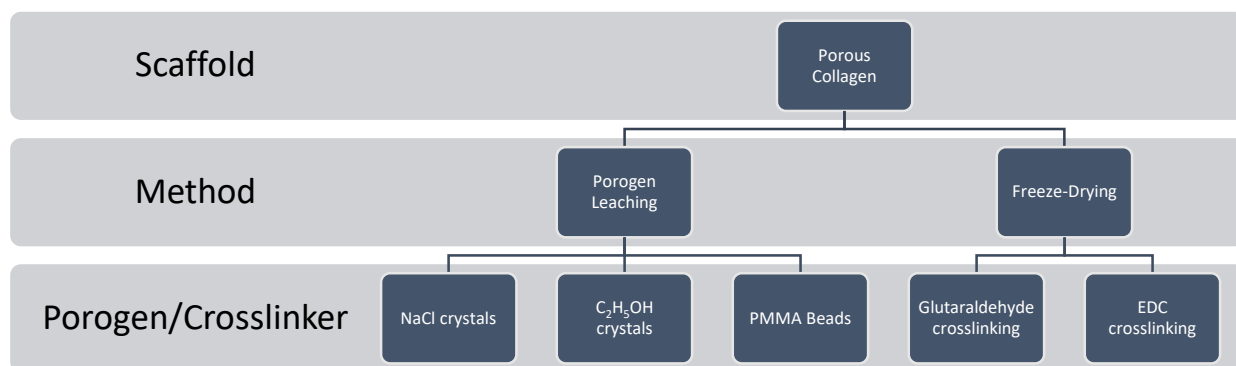


Figure 12: Development of porous Collagen type I divided into two porogen introducing techniques. These are further divided based on type of porogen or crosslinker used.

3.5.1 Porogen Leaching

Three different porogens were tested to develop porosities in Rat Tail Collagen type I gels (stock concentration 3.42mg/ml); PMMA beads, sodium chloride (NaCl) crystals and glucose (C₂H₅OH) crystals. Three sets of scaffolds were produced for each porogen having a V\W ratio of 75μl:55mg (Collagen I: Porogen), with a final Collagen type I concentration of 2.5mg/ml. The gels were crosslinked with THPC at a V\V ratio of 1:4 (THPC: Collagen I), with a stoichiometric ratio of 1:1, at a temperature of 37°C. The crosslinked gels were immersed in a solvent (THF 25% for PMMA beads and water for NaCl/glucose) for a day, followed by immersion into THF 100% for 3 days.

3.5.2 Freeze-Drying

The freeze-drying protocol was implemented on the following temperatures: i) -20°C, ii) -55°C and iii) -80°C. To develop a functioning protocol, initially the porous collagen scaffolds were frozen at -20°C only. The implemented freeze-drying protocols were adapted from Khayyatan, et. al., 2014 [21] and Park, et. al., 2002 [22].

According to Khayyatan, et. al., 150μl of Collagen type I gel with a final concentration of 2.5 mg/ml, was pipetted into the a well of a 96-well plate. The plate was then placed at -20°C for 2

hours, after which it was lyophilized at -55°C and 0.014 mBar for 24 hours. The lyophilized gels were then immersed into 0.6% glutaraldehyde for 24 hours at room temperature. The freeze-drying process was repeated for the crosslinked gels. Having lyophilized the re-frozen gels, they were hydrated with PBS.

The second method adopted from Park, et. al., 2002, followed a similar procedure with the following exceptions: a) HA, as purchased, was added to the collagen type I gel to provide additional structural integrity. It was added at a ratio of 8:2 (Collagen type I: HA, W/W). and b) the lyophilized gels were immersed in 50mM EDC dissolved in absolute ethanol, at room temperature for 24 hours.

3.6 Scaffold Characterization

3.6.1 Pore Size

The pore diameters were measured by fitting a circle (for porous ELP) or ellipses (for porous Collagen – HA) onto the pore formations, see figure 13. The longest diameter of the fitted shape was deemed as the diameter of the pore. A total of 50 pores for each porogen scaffold were measured. Other studies used similar measures to measure average pore diameters [22]–[24].

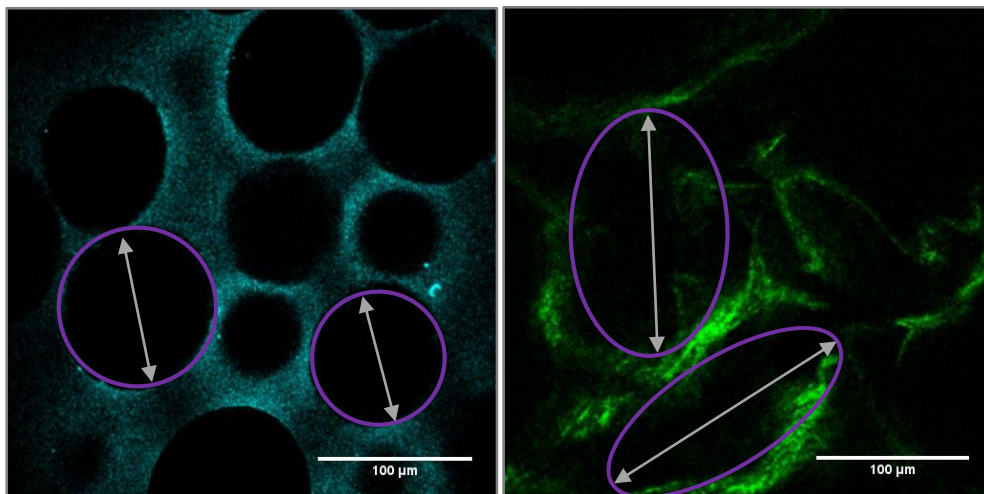


Figure 13: Circles or ellipses were fitted onto the imaged pores (in purple), and the largest diameter of these shapes was measured (in grey arrows).

3.6.2 Aspect Ratio

The aspect ratio is defined as the ratio between the long axis versus the short axis of the pore. A similar approach to that used to measure pore diameters was used to measure the aspect ratio. Circles (for porous ELP) or ellipses (for porous Collagen-HA) were fitted to represent the shape of the pore. The longest and shortest axis was then measured across the fitted shapes. A total of 50 aspect ratios were measured for each scaffold.

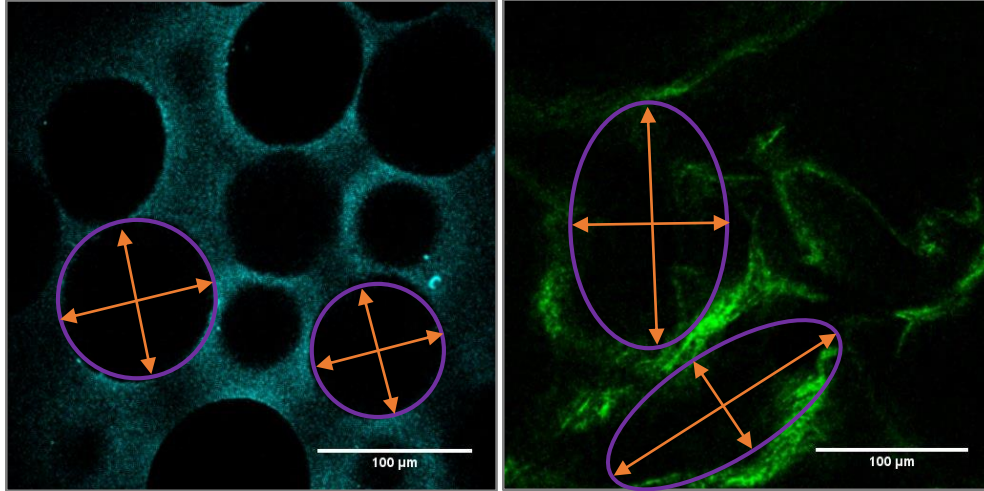


Figure 14: Circles or ellipses were fitted onto the imaged pores (in purple), and the largest diameter of these shapes was measured (in grey arrows).

3.6.3 Porosity

Porosity is defined as the percentage of void or empty space present within a material. Traditionally, porosity is measured using experimental techniques such as the gravimetric method, mercury porosimetry or liquid displacement method [23], [25], [26]; however, in this case image analysis techniques were implemented to provide a rough estimate of porosity.

Porosity was extracted by measuring the area fraction of 5 random images for each scaffold. Prior to calculating the area fraction; Gaussian blur with a radius of 2 was applied on the images to remove noise, and the resulting image was thresholded using an automatic thresholding algorithm (used Otsu's method) in imagej, see figure 15.

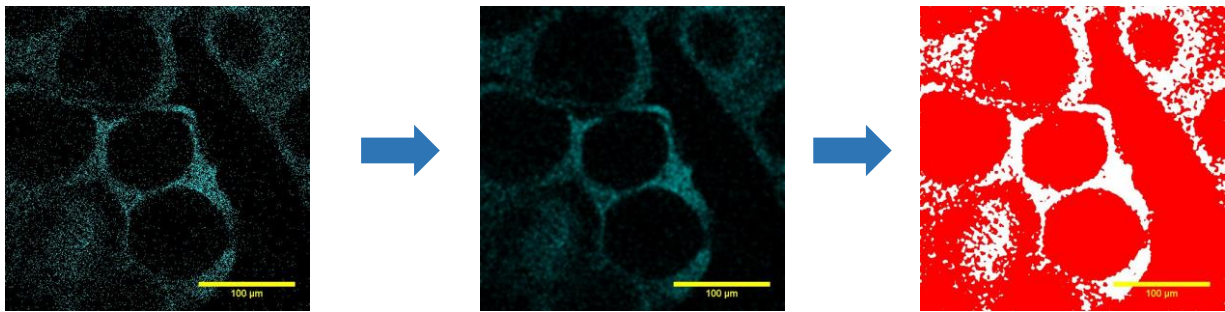


Figure 15: Step 1: A random image is taken. Step 2: Gaussian blur with radius 2 is applied. Step 3: Thresholding algorithm is applied. Step 4: Area fraction is calculated. Which is the percentage of pixels covered in the red region.

3.7 Cell Seeding Conditions

3.7.1 Cell Viability: Collagen Type I and ELP-RGD Coat

A 0.05 mg/mL Col-I in 0.02M acetic acid coating was formed by pipetting 25 μ l of it in wells of a 96 well-plate. The well plate was then incubated at room temperature for 45 minutes. After required incubation the mixture was removed and wells were washed with PBS. The coated wells were stored in PBS at 4°C until use.

The ELP-RGD coat was made in a similar manner as the Col-I coat. ELP-RGD with a working concentration of 0.05mg/ml in PBS, was pipetted into wells of a 96 well-plate. The well plate was kept at 4°C overnight. The mixture was then removed, and wells were washed with PBS and stored at 4°C in PBS until use.

A total of 125 cells/mm² were seeded per well. The cells were stained with Live/dead assay (ThermoFisher Scientific).

3.7.2 Cell Encapsulation: Collagen Type I and ELP-RGD

MDA-MB-231 cells were encapsulated in Col-I with a working concentration of 1.5mg/ml. The encapsulations were made in a 96 well-plate by pipetting 50 μ l of Col-I and Sodium Hydroxide mixture having a homogenous distribution of cells. The gels were then incubated at 37°C for a period of 2 hours after which additional medium was added.

The ELP-RGD encapsulations was made in a similar manner to the Col-I encapsulation. With ELP-RGD concentration as 30mg/ml, and the gel crosslinked with THPC at a stoichiometric ratio of 1:1.

A total of 500cells/ μ l per encapsulation were seeded. The cells were stained with Cell Tracker Red CMTPX at working concentration of 5 μ M.

3.7.3 Porous Collagen I-HA Scaffold

Two different techniques were tested when seeding MDA-MB-231 cells on the porous Collagen I-HA. The first technique involved seeding of 450,000 cells in 150 μ l of medium, whereby the cell seeding solution is gently and slowly pipetted on the scaffold. The second technique involved seeding 300,000 cells in 1000 μ l medium. A gentle flow was created through the porous scaffold by placing the scaffold within the pipette tip, and drawing the cell seeding solution through it. This was repeated 3-4 times to ensure optimum presence of cells in pores.

The fixed samples were stained with Alexa Fluor 488 Phalloidin at a final concentration of 6.6 μ M. While, for live-imaging, the samples were stained with Cell Tracker Red CMTPX at a final concentration of 5 μ M. Both stains were used to visualize the cells within the scaffold.

3.7.4 Porous ELP-RGD Scaffold

The outlined two techniques were translated into the porous ELP-RGD seeding. The first technique used 30,000 cells seeded in 5 μ l of medium, and a period of 2 hours was provided for the cells to

adhere to the scaffold before addition of medium. The second technique involved seeding 300,000 cells in 1000 μ l; the same procedure as for porous Collagen I-HA was followed.

3.7.5 Nanowrinkle ELP Scaffold

A total of 442 cells/mm² were seeded per well. The cells were allowed to attach to the substrate for 2 hours after which 150 μ l of medium was added.

For live-imaging the samples were stained with 5 μ M Cell Tracker Red CMPTPX, while fixed samples were stained with Alexa Fluor 488 Phalloidin at a final concentration of 6.6 μ M.

3.8 Multi-modal Nonlinear Microscopy

A multi-modal nonlinear microscope was used for the purpose of imaging samples. The setup schematic is outlined in figure 16. Briefly, a picosecond pulsed laser system (Picotrain, HighQ Lasers GmbH) is coupled with an inverted microscope (Eclipse TE-2000, Nikon) equipped with a beam scanner. The laser system emits at wavelengths of a) 1064nm and b) 532nm. The 532nm beam is then guided into an Optical Parametric Oscillator (Emerald OPO, APE GmbH) which produces a tunable output beam in the near-infrared region of 690-990nm. All images have been captures either with a beam at 811nm or 817nm, unless specified otherwise. Both the 1064nm and 811/817nm beams are overlapped in space and time; after which they are guided into the microscope. The setup has three different detectors; a) the forward detector b) the epi-side detector and c) the epi-back detector. Depending on the combination of filters, and excitation wavelengths used; the system is able to detect different properties, characteristics of the sample.

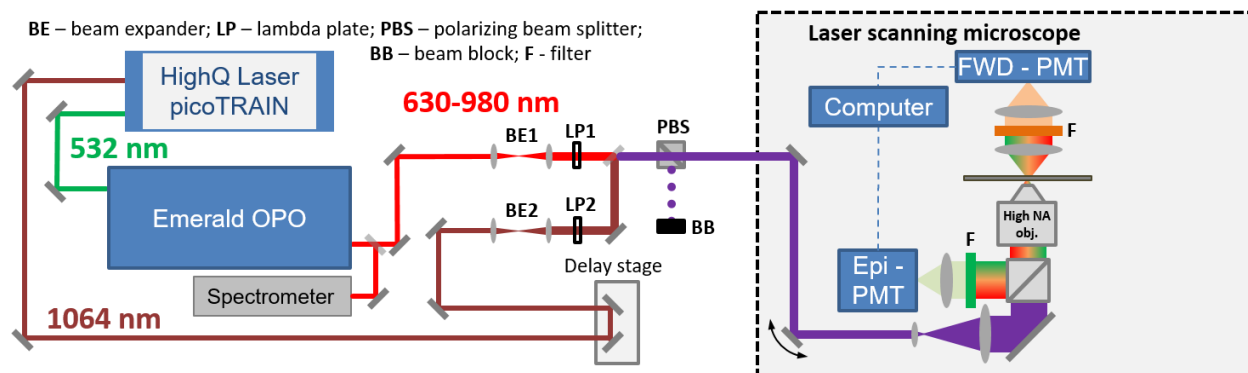


Figure 16: Schematic representing optics in the microscopy setup. The optical pathway of both beams, 1064nm and 532nm, is shown. The detectors have been condensed into forward detector (FWD-PMT) and the two epi detector (Epi-PMT).

The microscope was controlled with Nikon software EZ-C1. While DCC and SPCM, developed by Becker & Hickl, were used to control the detectors and signal collection respectively. Brightfield images were acquired with Optikaview. All collected images have pixel size of 512 \times 512 pixels with pixel dwell of 3.12 μ s unless stated otherwise. Further, all compared images have the same settings on gain, exposure times and laser powers (30mW - 50mW).

3.8.1 Imaging: Fluorescent Stains

All fluorescence signals from stains were excited with 817nm beam and signals were detected in EPI. The stains in combination with the filters (Semrock) used are listed in table 2.

Table 2: The stains used alongside the respective filter combinations used with the stains. All signals from stains represented were detected in EPI.

| Stain | Filter |
|----------------------------|--------------------|
| Cell Tracker Red | 609/57nm |
| Live/Dead Assay | 514/30nm, 609/57nm |
| Alexa Fluor 488 Phalloidin | 514/30nm |

3.8.2 Imaging: SHG and CARS

The SHG signals were excited with both the 817nm and 1064nm beam, and were captured in Epi. On the other hand, CARS was excited with the 811nm and 1064nm beam, and was captured in the Forward detector. The filters used for SHG signals were 405/10nm, and for CARS signals were 661/20nm.

4 Results and Discussion

4.1 Scaffold Development

The criteria used to evaluate the successful formation of porous ELP and porous Collagen gels were the following: a) the integrity of gels, i.e. the swelling of scaffold without collapse of pores when rehydrated b) qualitative pore formation.

4.1.1 Porous Elastin-Like Polypeptide Scaffolds

The ELP: PMMA (v/w) ratio of 90:55 provided both overall structural integrity and adequate pore formation. All further characterization was performed using this ratio. An important parametric to assess the development of porous ELP scaffolds is complete removal of PMMA beads. This was judged through CARS microscopy. The chemical specific microscopy technique tapped into the vibrational mode of methyl groups; which were present within the PMMA beads. The technique allowed distinction between PMMA beads, figure 17a, and autofluorescence from ELP to visualize pore formation, figure 17b.

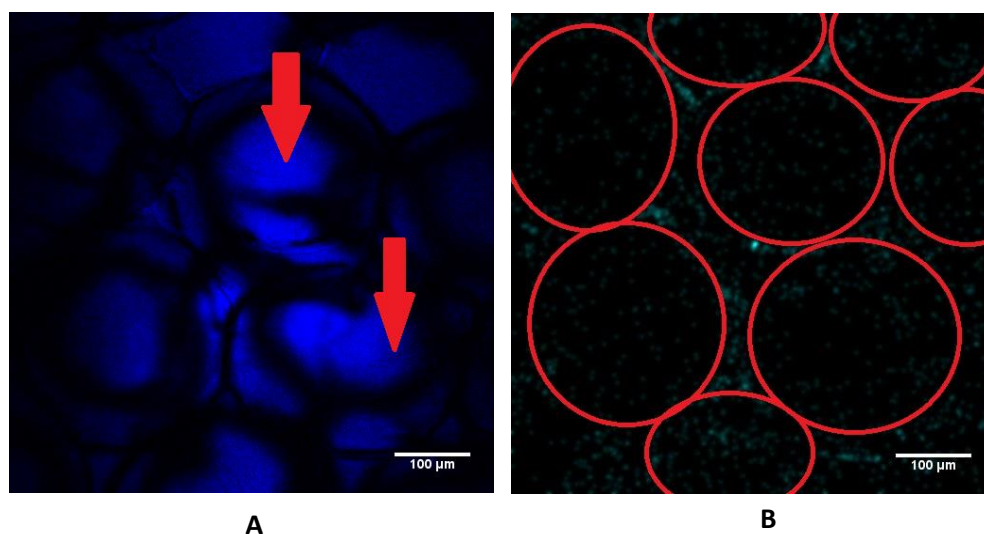


Figure 77: CARS and fluorescence images of the 90:35 gel (A) The CARS image. The presence of PMMA beads is clearly visible, and marked with arrows. (B) The fluorescence image. The pores formed are outlined with red circles for visibility.

The pores formed through porogen leaching generated pores with a regular, spherical shape, see figure 18. The diameter of the porogens governed the diameter of the produced pores. The diameter of the porogens was chosen with respect to the average diameter of MDA-MB-231 cells, which is 10μm to 20μm [27]. The porogen diameters were a) 20-27μm, that is the diameter of MDA-MB-231 cells b) 106-125μm, the diameter of an elongated cell and c) 250-300μm, representing a diameter greater than an elongated cell. The variation pore diameter could provide the cell cues to adopt a certain morphology; that is round or elongated morphology.

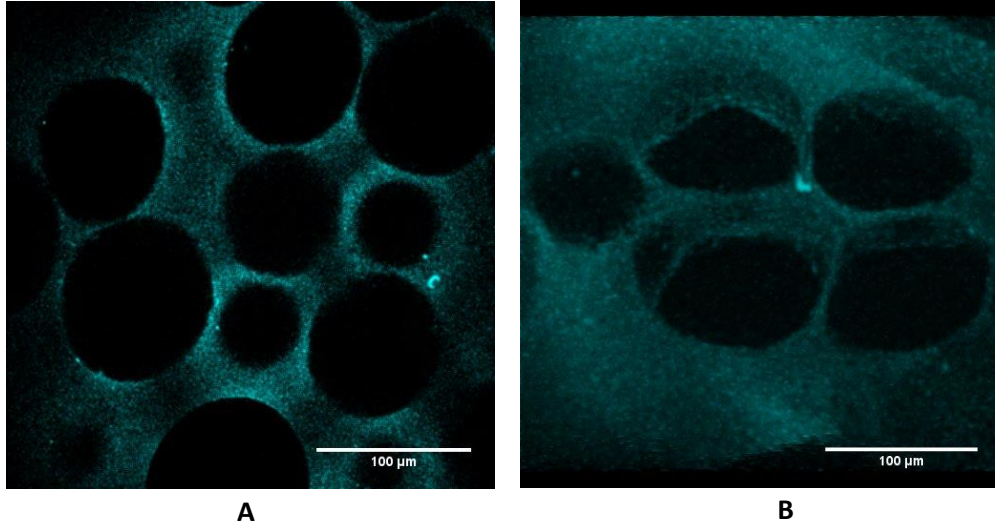


Figure 18: The fluorescence images from porous ELP-RGD. The circular pore formations are visible in (A). A 3D rendered pore is shown in (B). The pore forms a spherical shape, which is takes the shape of the porogen.

4.1.1.1 Scaffold Characterization

The porous ELP-RGD scaffolds developed were measured to be 7mm in diameter and 0.5mm in thickness. Other properties measured were the pore sizes, aspect ratio and porosity.

4.1.1.1.1 Pore Size

The diameter of the pores depended on the diameter of the porogen. The PMMA beads used to create the pores, had diameters between 20-27µm, 106-125µm and 250-300µm. The average pore diameters measured represented this information. The porogen leaching technique permitted

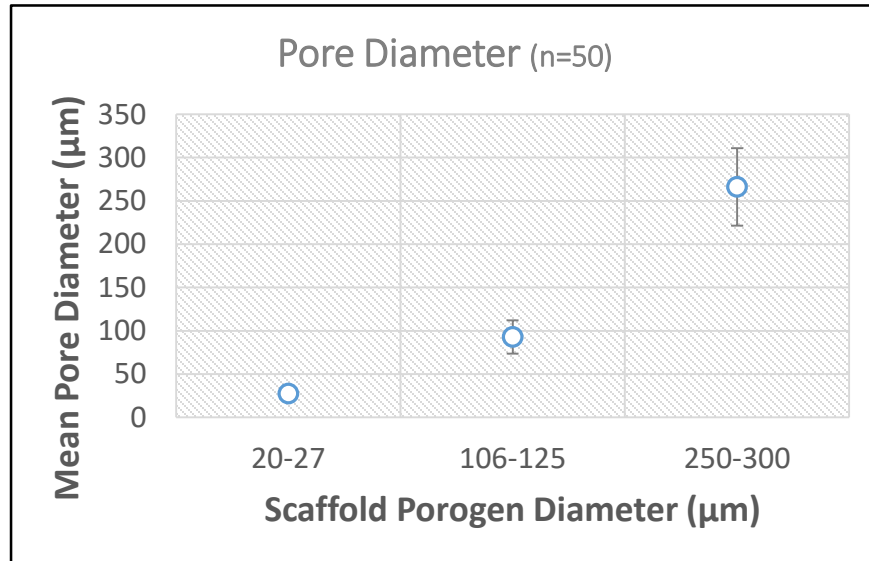


Figure 19: The measured mean pore diameter (+/- SD) versus the porogen diameter of scaffold. The mean pore measure pore diameter is represented with standard deviations.

control over the pore diameters. Control over the pore diameters allowed reasonable conclusions to be made on the correlation between pore diameters and cell morphology adopted by cells.

4.1.1.1.2 Aspect Ratio

The pores formed in porous ELP can be approximated to have a circular cross section. The aspect ratio measured for the porous ELP-RGD scaffolds is represented in figure 20. Since, the pore formations are spherical in nature, the diameter across both larger and shorter axes was estimated to be similar. As expected the aspect ratio for all three scaffolds varies around 1.

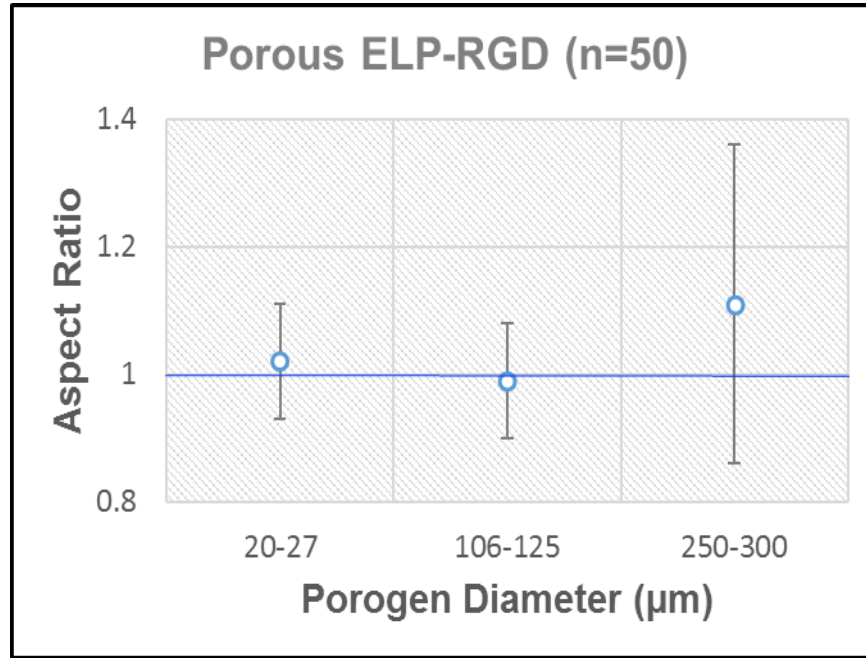


Figure 20: The aspect ratios of all three scaffolds vary around the 1 (+/-SD). Reinforces the fact that the cross sectional shape of the pore for all scaffolds is circular.

4.1.1.1.3 Porosity

The porosity of a scaffold is an important parametric. Scaffold porosity determines whether adhered cells have sufficient flow of medium. The porosity of the porous ELP-RGD scaffolds was measured by image analysis techniques, as outlined in methods. Briefly, the porosity was measured by calculating the area fraction of a total of 5 random images per porogen diameter.

The data shows that all porous ELP-RGD scaffolds have porosities greater than 90%, figure 21. Other studies measured porosities of 99% on average [23], [26]. However, it must be noted that these studies implemented experimental techniques to measure porosities. A comparable study that implemented image analysis techniques stated scaffold porosity to be an average of 60% [22]. Due to the physical limitations (diffraction limit), the spaces between individual ELP cannot be imaged. Which contributes towards overall porosity of the scaffold. The experimental techniques measure porosity as a volumetric element, while the image analysis techniques implemented treated porosity as area element. The true porosity of a scaffold can be measured by considering the pores as volumetric element, thus the experimental techniques provide a better estimation on porosity. Even though, the calculated, estimated porosities were in excess of 90%, the true porosity of the scaffold would be higher.

A trend is noticeable between the three scaffolds. The porosity increases with increasing pore diameter. The largest porogen diameter is 250-300 μ m, and subsequently, the highest porosity is also of the 250-300 μ m scaffold. While the smallest porogen diameter is 20-27 μ m, and the lowest porosity is of the 20-27 μ m scaffold.

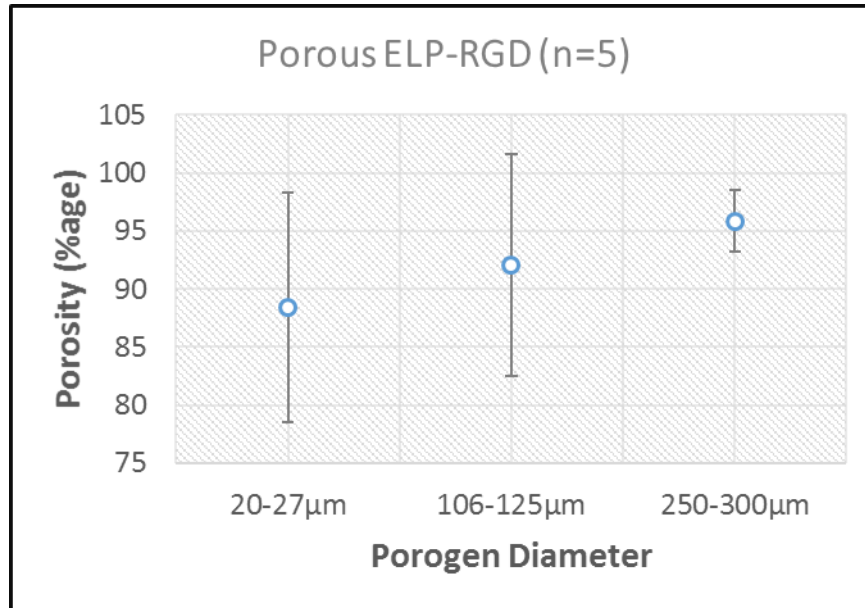


Figure 21: The porosities measured for all three porous ELP-RGD scaffolds (+/- SD). The scaffolds have porosities greater than 90 percent. The scaffolds with porogen diameters 20-27 μ m and 250-300 μ m had the lowest porosities at 94 percent, while the 106-125 μ m porogen scaffold have the highest porosity with 98.6 percent.

4.1.2 Porous Collagen type I - HA Scaffolds

4.1.2.1 Developing the protocol

4.1.2.1.1 Porogen Leaching

As described in materials and methods, three different porogens were tested to produce porosities in Rail Tail Collagen type I gels. As an initial test, the technique honed for producing porous ELP-RGD gels was translated onto producing porous Collagen I gels with PMMA beads. The Collagen I gel successfully crosslinked, with the PMMA beads embedded in it. However, immersion of the gel in THF 25% caused the collagen I gels to disintegrate. This was expected since, THF is classified as an organic solvent, and Col-1 will have dissolved in THF. The second porogen leaching approach encompassed use of NaCl crystals to act as porogens [28]. The inclusion of the crystals caused an ionic imbalance which adversely affect the collagen fibril formation [29]. Subsequently, the lack gelation and crosslinking was due to failure of fibril formation. Following this, the third porogen used was glucose crystals. It was known that glucose crystals would not cause an ionic imbalance; however, were highly soluble in acetic acid. The glucose crystals solubilized in acetic acid present present within the Collagen I solution during incubation. A second attempt was made to saturate the solution with glucose prior to incubating. However, the Collagen I solution failed to gel. Having tried three different porogens, the approach failed to materialize towards usable and reproducible results.

4.1.2.1.2 Freeze-Drying

Two methods were tested to develop freeze-dried porous Collagen I gels; method A by Khayyatan, et. al., 2014 and the method B by Park, et. al., 2002. The porous Collagen I gel produced by method A, seemed to have successfully crosslinked with glutaraldehyde. However, after the second lyophilization and rehydration in PBS, the crosslinked gel lost its macro structure. The gel collapsed; which indicated poor crosslinking within the porous construct [23]. The crosslinking mechanism can be reinforced by introducing glycosaminoglycans (GAGs) within the Collagen I mixture.

Briefly, method B introduced hyaluronic acid into the porous Collagen I gel, as a means to structurally reinforce the scaffold. Further, the scaffold was crosslinked with EDC prior to the second freeze-drying cycle. The gels produced with this method retained their structural integrity throughout the process and visibly displayed porous elements. This was confirmed with SHG microscopy, see figure 22.

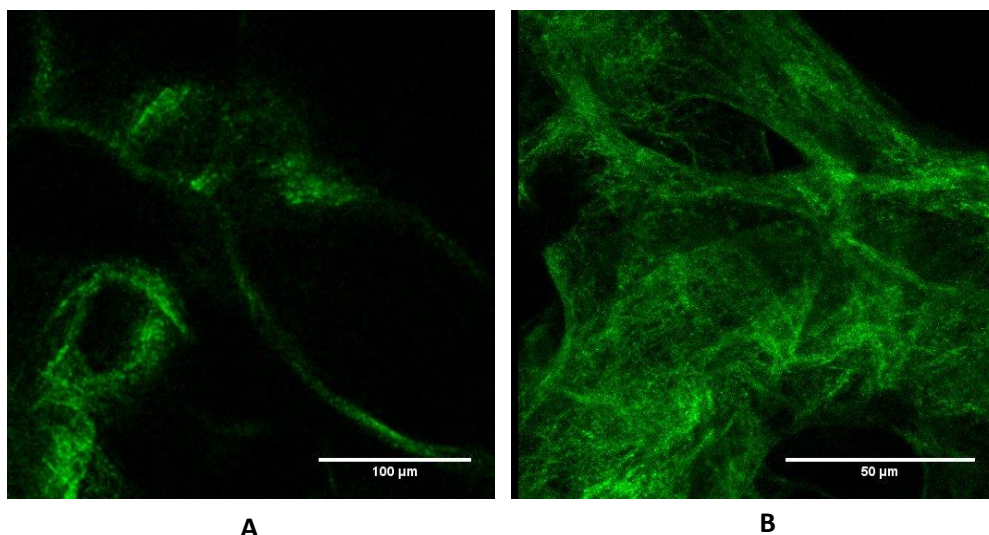


Figure 22: SHG images of the formed porous collagen-HA gel with method B. Signal is generated from the Collagen-HA walls, whose intricate network form the porosity. **(A)** Scaffold produced at final temperature of -20°C . **(B)** A 3D projection of SHG signal from porous Collagen-HA (-55°C). The freeze-drying process forms interconnected, irregular pores.

4.1.2.2 Scaffold Characterization

The porous Collagen I – HA scaffolds had dimensions of 4mm by 5mm (height by diameter). All scaffolds produced showed a three-dimensional porous structure. The pores inside the scaffolds were interconnected in irregular patterns, and the pore sizes varied with the freezing temperature. The scaffolds were characterized by the pore sizes produced versus the freezing temperature, the aspect ratio of the pores and porosity.

4.1.2.2.1 Pore Size

The scaffolds were produced at three distinct final freezing temperatures; -20°C , -55°C and -80°C . A total of 50 pores per scaffold were measured to evaluate the mean pore size, summarized in figure 23. The scaffolds formed at a final temperature of -20°C had the largest pore size with mean pore size of $240\mu\text{m}$. As the freezing temperature dropped, the mean pore diameter decreased as well. The mean pore sizes at -55°C and -80°C had similar values of $90\mu\text{m}$ and $77\mu\text{m}$, respectively. An additional parameter that influences nucleation of ice crystals is humidity. Similar humidity levels in the freezing environment for the scaffolds produced at -55°C and -80°C could be the reason behind similar measured pore sizes.

The data reveals that the final freezing temperature influences the pore size of the scaffold, which was concurrent with other studies [30]. Further, the pore sizes followed the trend outlined in literature; decreasing final freezing temperature causes the mean pore diameter to decrease [22], [24]. The final freezing temperature modulates the rate of nucleation of ice crystals (which serve as porogens), and the rate of heat and protein diffusion [30], [31]. With a larger undercooling temperature, difference between final freezing temperature and actual temperature of scaffold, the rate of ice crystal nucleation increases and decreases the rate of heat and protein diffusion. The

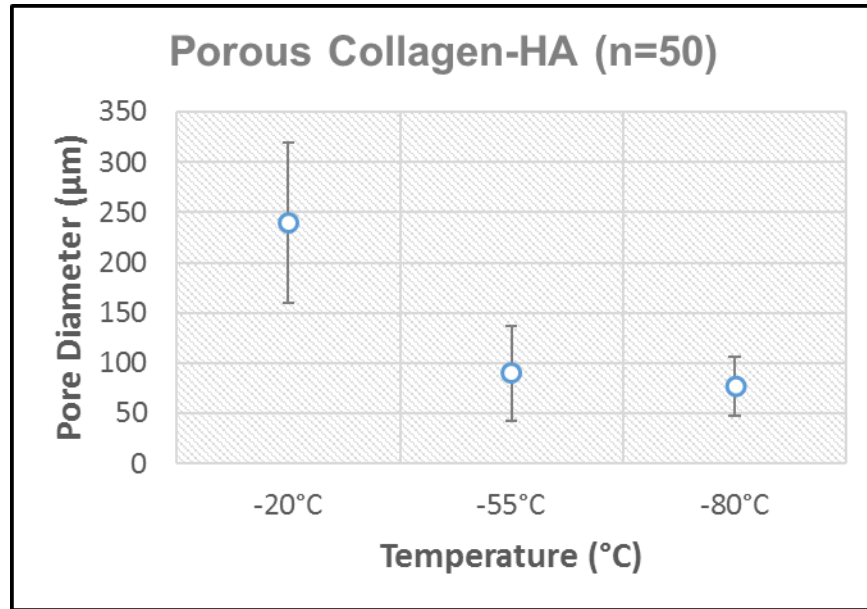


Figure 23: The measured average pore diameter (\pm SD), for all three scaffolds developed at three distinct final freezing temperatures.

difference in pore diameters at decreasing temperatures is evident of varying ice crystal nucleation rates and heat transfer rates during the freezing process; which points towards successful formation of porous Collagen-HA scaffolds.

4.1.2.2.2 Aspect Ratio

The pores generated in the scaffolds have an irregular, complex shape with high interconnectivity; similar to lung parenchymal tissue present *in vivo*. However, the pores can be approximated to an elliptical shape; as was outlined in materials and methods. Keeping this assumption, the aspect ratio of 50 pores were measured, see figure 24.

The aspect ratio of a perfect circle is 1; as indicated by the blue line in figure 24. Values greater than 1 indicate the elliptical nature, and indicate how far the shape varies from a perfect circle. The pores formed at each of the scaffold freezing temperature held aspect ratio greater than 1; this indicated that the pores had a flattened, elliptical shape. In comparison to the porous ELP aspect ratio, where the values mirrored around 1, the elliptical nature of porous Collagen-HA pores mimic *in vivo* conditions better. However, the controlled nature of porous ELP pores permits a rather controlled structural interaction between pore diameters and cell morphology.

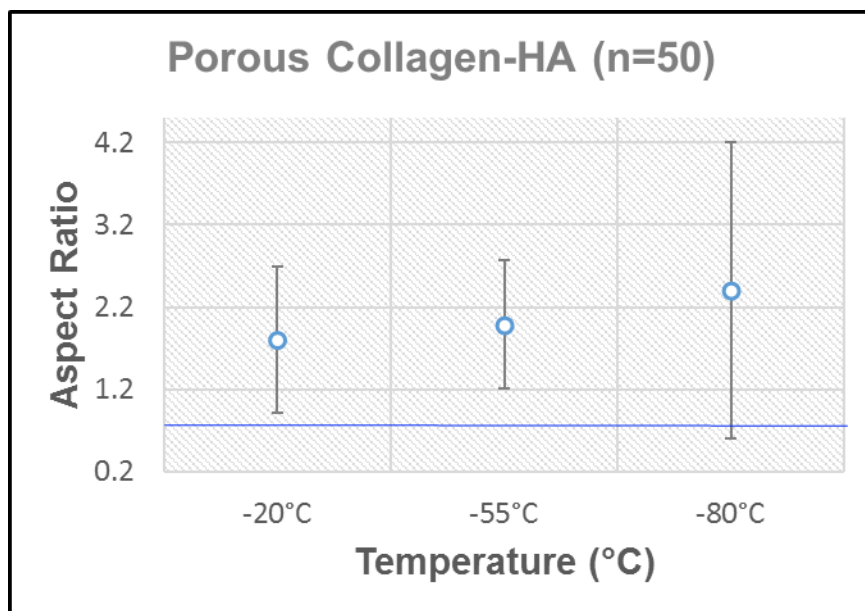
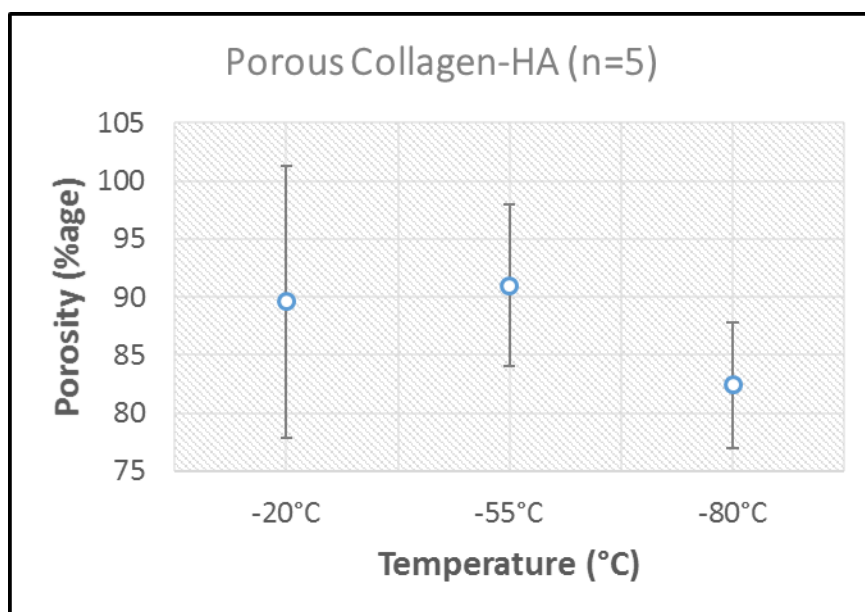


Figure 24: The aspect ratio of scaffolds produced at all three freezing temperatures (+/- SD) was greater than 1; indicating that the pores greatly deviated from circular morphology.

4.1.2.2.3 Porosity

The porosities of the porous Collagen-HA scaffolds were measured using the same image analysis techniques that were used to measure porosities for porous ELP-RGD. All porous collagen-HA scaffolds were measured to have porosities greater than 80 percent, figure 25. As with porous ELP scaffolds, the true porosity of the porous Collagen-HA scaffolds is speculated to be higher.



4.1.3 Nanowrinkle ELP Scaffold

The wrinkled surfaces mimic the two-dimensional surface topography of *in vivo* structures; such as blood vessels. Further, the 1D substrates mimic the alignment of Collagen fibers on the invasive tumor front. Nanowrinkle ELP scaffolds with periodicity of $4.5\mu\text{m}$, $3.7\mu\text{m}$, $1.4\mu\text{m}$ and flat surface were used, see figure 26. The difference between 1D and 2D nanowrinkles is clearly visible in

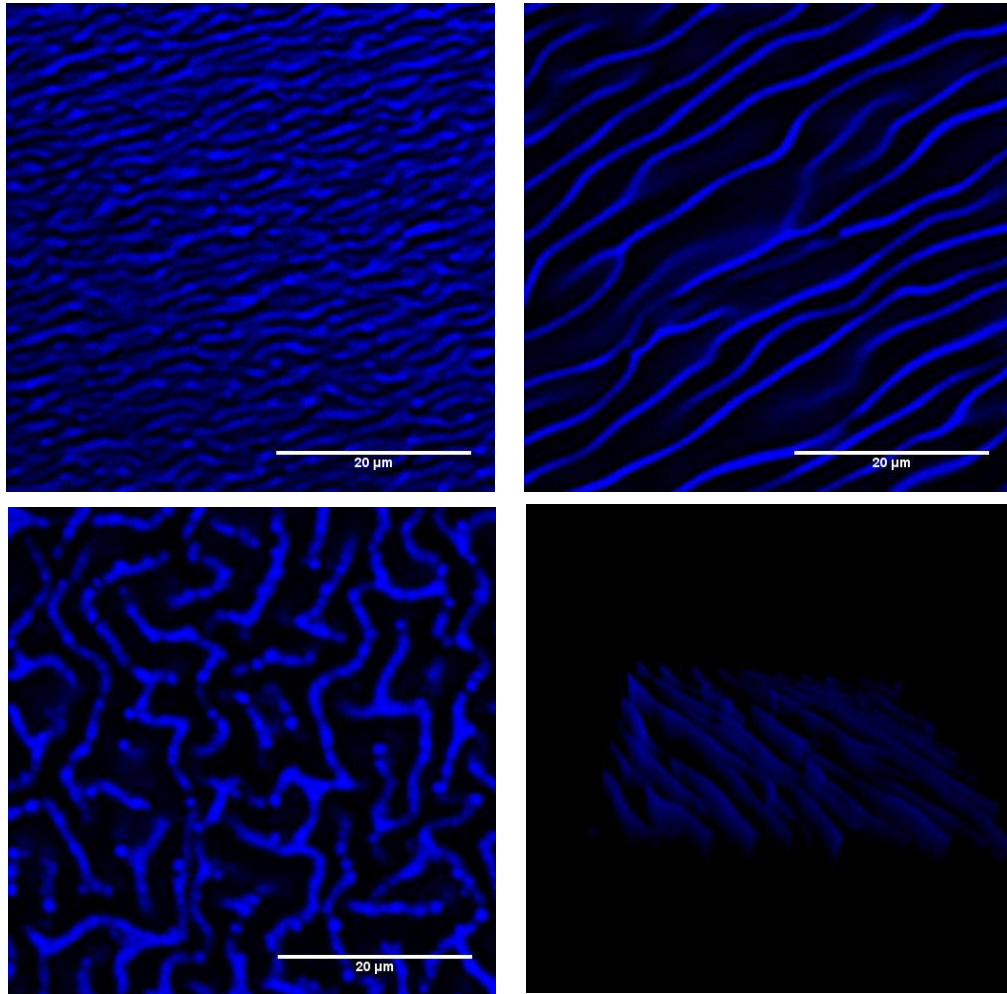


Figure 26: The CARS images of the three different nanowrinkles produced. The top-left and top-right images represent the 1D wrinkles while the bottom-left image is of 2D wrinkles. The bottom-right image shows a 3D reconstruction of a nanowrinkle. (TL) The $1.6\mu\text{m}$ nanowrinkle with CARS microscopy (TR) The $1\text{D } 3.7\mu\text{m}$ nanowrinkle (BL) The $2\text{D } 4.7\mu\text{m}$ nanowrinkle (BR) $1\text{D } 1.4\mu\text{m}$

figure 26; where the 1D nanowrinkles are highly ordered and the 2D nanowrinkles have an inherent disorientation.

4.2 Cell Studies

The viability of MDA-MB-231 cells on both ELP-RGD and Col-I was tested in a three tier process. First, the cells were seeded onto a coat consisting of each material. The purpose of which was to investigate cell adhesion and toxicity of the materials. The second tier, was to check their viability in a 3D environment. This was performed by encapsulating the cells in ELP-RGD and in Col-I gel. The third and final step, was to introduce topographical traits into the 3D environment. The behavior of the cells on pores and nanowrinkles was then studied.

4.2.1 Cell Viability on 2D Substrates: Collagen Type I and ELP-RGD

MDA-MB-231 cells were seeded onto both Col-I and ELP-RGD coats. The purpose of the coats was to establish viability of the cells on both materials. The cells were incubated for a total of 48 hours; with the live/dead assay performed after 24 hours and 48 hours after incubation.

The cells seeded onto Col-I coat adhered well to the substrate after 24 hours; as was visible by the elongated nature of the cell morphology, figure 27. After 48 hours after seeding, the cells seemed to have proliferated and displayed signs of attachment. Furthermore, the lack of signal from the ethidium homodimer-1 suggests that cell death was next to non-existent at both 24 hours and 48 hours after seeding. The result reinforced the thought that the cells adhere well to the Col-I substrate, which is also supplemented by literature[32]–[34].

In contrast, the cells seeded on the ELP-RGD coats had not adopted an elongated morphology after 24 hours of incubation. A strong signal was detected from calcein-AM, indicating that although the cells had rounded morphology they were alive. However, 48 hours after the seeding, a marked difference was noticed. The cells possessed an elongated morphology which was an indication of cell integrin attachment to the RGD sequence within ELP-RGD. This was speculated and was concurrent with literature [35]. Additionally, a cluster of cells is noticed both 24 hours and 48 hours after seeding. Possibly, cell-cell interactions influenced the attachment of cells onto

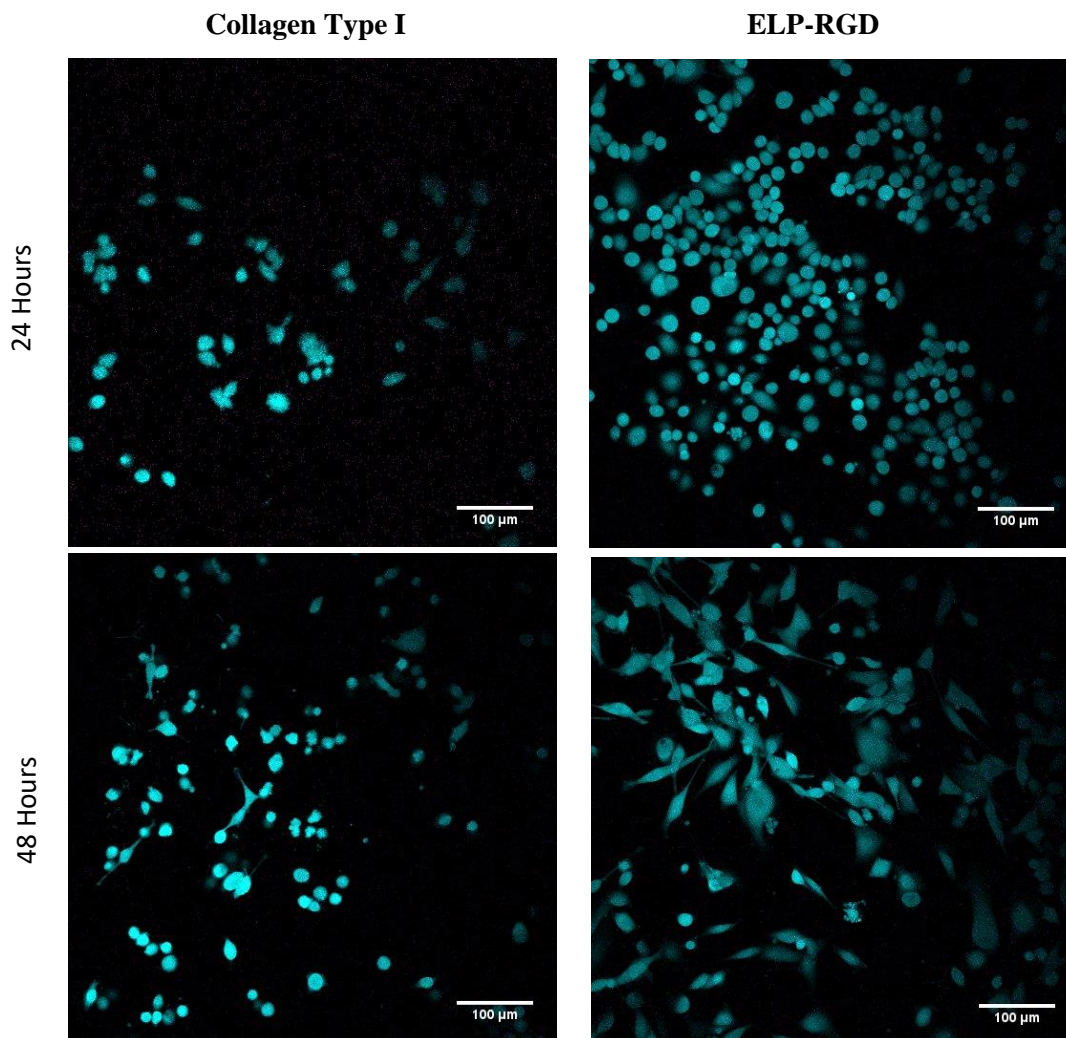


Figure 27: MDA-BM-231 cells were seeded onto both Col-I and ELP-RGD coats. Cells were stained with live-dead assay and imaged after 24 and 48 hours of incubation. Both conditions showed live, adherent cells after 48 hours of incubation.

the ELP-RGD substrate or the cells secreted their own ECM components to facilitate in cell attachment.

4.2.2 Cell Viability in 3D Substrates: Collagen Type I and ELP-RGD Encapsulation

Having determined the viability of MDA-MB-231 cells on two-dimensional Col-I and ELP-RGD coats, the next step was to assess their viability in a three-dimensional environment. The three-dimensional environment serves as a closer *in vitro* model; considering that cells *in vivo* are stimulated in a three-dimensional environment. Cell viability in three-dimensions was investigated by encapsulating the cells in Col- I and in ELP-RGD.

As with cell viability on 2D coats, MDA-MB-231 cells adhered well to the Col-I, see figure 28. Results gathered 24 hours after seeding show that the cells had elongated morphology; indicating that they had formed focal adhesion sites and adhered well to the substrate. The cells possessed the same elongated morphology after 48 hours of incubation. Due to the lack of signal from the

ethidium homodimer-1, it was speculated that cells did not lyse in their three-dimensional environment. Conclusively, the MDA-MB-231 cells were compatible with Collagen type I.

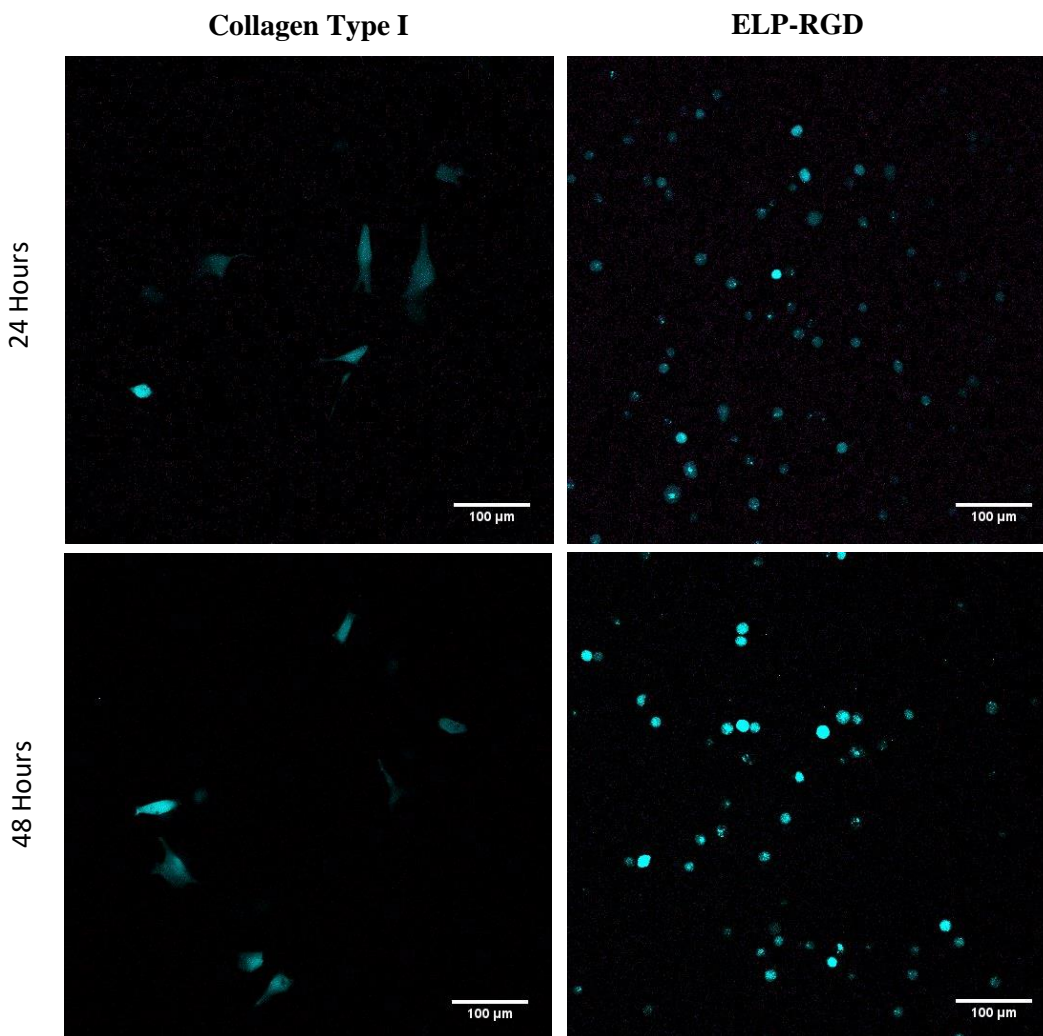


Figure 28: MDA-BM-231 cells were seeded onto both Col-I and ELP-RGD encapsulations. Cells were stained with live-dead assay and imaged after 24 and 48 hours of incubation. The cells in the Col-I encapsulation adopted elongated morphology after 24 hours of incubation. While, cells in the ELP-RGD encapsulation kept a rounded morphology even after 48 hours of incubation. It must be noted that cells in both conditions were live.

Alongside the Collagen type I encapsulation, a parallel investigation was carried out on the viability of MDA-MB-231 cells in a three-dimensional ELP-RGD environment. As before live/dead assay was performed 24 hours and 48 hours after seeding. After 24 hours the encapsulated cells had rounded morphology. The cell morphology remained the same 48 hours after seeding. The strong signal from calcein-AM indicates that the cells survived in the ELP-RGD environment. However, the rounded morphology suggests that cells did not formed focal adhesion

sites with the substrate. It was speculated that the cell death would occur, since, the lack of focal adhesion points to the substrate is known to initiate apoptosis [36].

Though, the cells proved viable on a two-dimensional ELP-RGD coat; their viability in a three-dimensional ELP-RGD environment was questionable. The behavior of the cells in the three-dimensional ELP-RGD environment can be explained through the toxicity of the cross linker, THPC. The latter could adversely interact with the cells causing the cells to ‘dislike’ their otherwise ‘likeable’ environment, further investigation needs to be carried to assess toxicity of THPC. Another possible explanation, is that the cells required incubation beyond 48 hours. As was observed with cells on the ELP-RGD coat, where cells adhered to the substrate after 24 hours.

4.2.3 Porous and Nanowrinkle Scaffolds

4.2.3.1 Porous Collagen-HA

Two different seeding techniques were implemented to seed cells into the porous constructs. The first technique involved seeding a high number of cells in a small amount of volume. The seeding solution was gently pipetted onto the porous Collagen-HA scaffolds. After an incubation time of 24 hours and addition of more medium, it was noted that the cells had passed through the pores, and adhered to the well. The second seeding technique, involved creating a gently, turbid flow through the porous construct with the cell seeding solution. Incubating the scaffold at 37°C for 2-3 hours, and adding additional medium in the well. This seeding technique proved effective, and after cell were found within the pores after an incubation time of 24 hours.

MDA-MB-321 cells were seeded on porous Collagen-HA scaffolds that were prepared at three different temperatures; at -20°C, -55°C and -80°C, see figure 29. The purpose of seeding cells onto three different scaffolds was to assess the effect of varying pore size on cell behavior. A large populous of cells were found within all three porous constructs; which reinforced the effectiveness of the second seeding technique. The cells attached to the Collagen-HA walls in all three scaffolds.

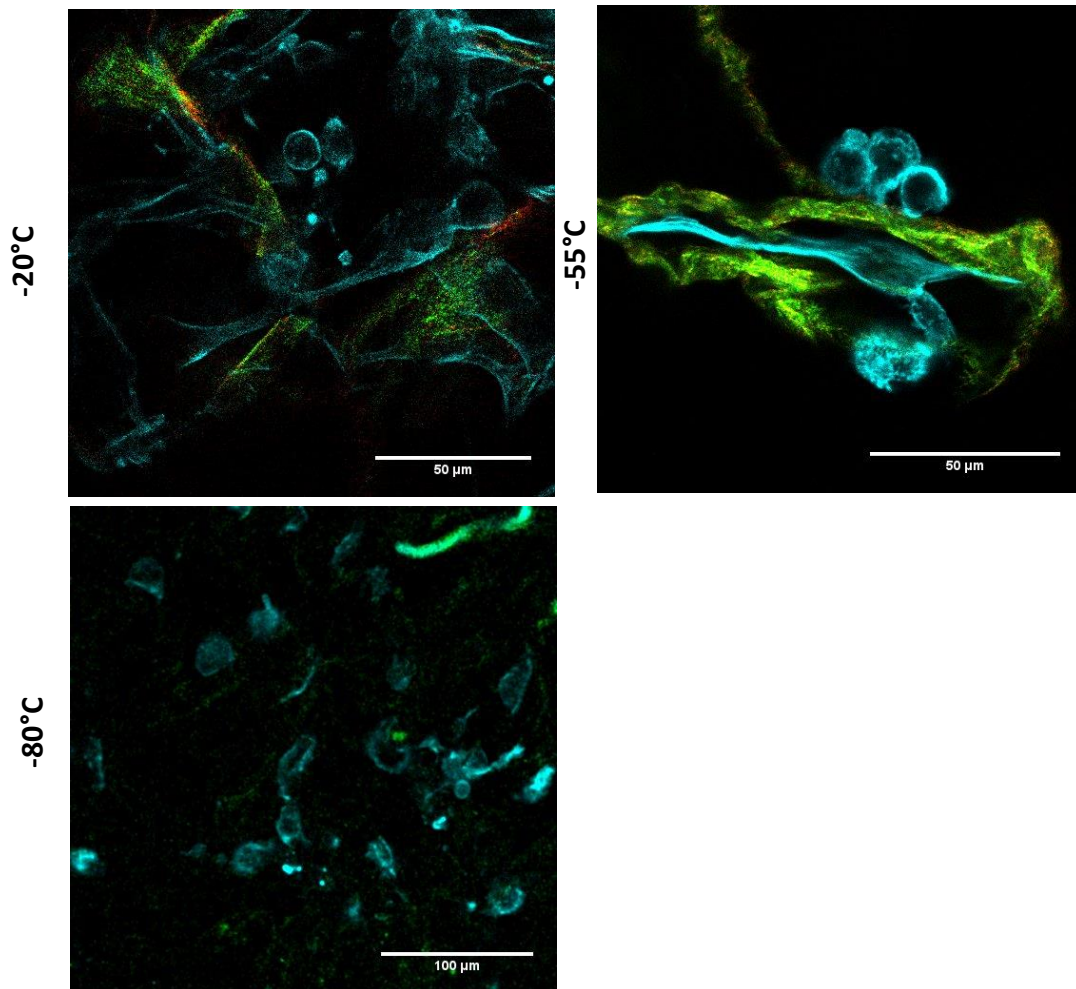


Figure 29: Fluorescence and SHG images of seeded porous Collagen-HA scaffolds. The cells are within the pores, and either have rounded or elongated-like morphology.

All three porous Collagen-HA scaffolds had cells with either rounded morphology or elongated morphology. Cells with rounded morphology had their cell body in a round, circular shape and were attached to the pore boundary; as seen in figure 30. Elongated morphology is characterized by cells having a long polarized cell body, with the cell stretching across the pore boundary, also marked in figure 30.

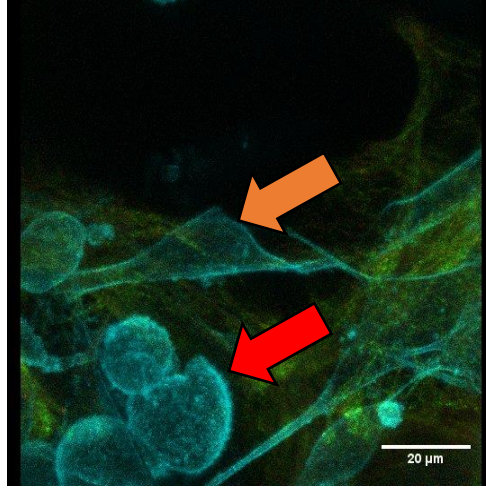


Figure 30: A 3D projection of cells in -55°C scaffolds. The red arrow marks cells with rounded morphology. The orange arrow marks cells with elongated-like morphology. The green and red signal is of SHG from Col-I, while the cyan represents fluorescence from actin stained cells.

The scaffolds produced at -20°C , having an average pore diameter of $240\mu\text{m}$, had a large number of cells with rounded morphology. Studies indicate that cells can reach an average maximal polarized length of $100\mu\text{m}$ [8]. To reinforce this statistic, the cell diameter, from one focal adhesion site to the other, was measured for 10 cells with elongated-like morphology. An average elongated-like cell diameter of $90\mu\text{m}$ was measured. The latter correlates with the existing studies, and explains the abundance of cells adopting the rounded morphology. The average pore diameter of $240\mu\text{m}$ proved to be a physical hindrance for the cells, which were then coaxed into adopting the rounded cell morphology. The scaffolds produced at -55°C and -80°C had cells exhibiting similar characteristics. This was expected since the two scaffolds had similar average pore diameters; with the -55°C scaffold having a pore diameter of $90\mu\text{m}$ and the -80°C scaffold having a pore diameter of $77\mu\text{m}$.

The cells formed the elongated-like cell morphology within pores whose pore diameter was similar to maximum cell polarization length. This reinforced the findings regarding cell morphology and pore diameters from the -20°C scaffolds. It was noted that pores where the pore diameter was below $40\mu\text{m}$; the cells opted to adopt rounded morphology. The results uncovered through these studies reveal that the pore size have an effect on the morphology of the cells, see figure 31. The elongated-like morphology of the cell is depended on whether the pore acts as a physical constraint or support. If the pores are too small, below $40\mu\text{m}$, or too large greater than $90\mu\text{m}$; the cells lean towards adopting rounded morphology. With pore sizes between $40\mu\text{m}$ and $90\mu\text{m}$; the cells tend to form elongated-like morphology. These tendencies to form a particular type of cell morphology, influence the mode of cell migration[7].

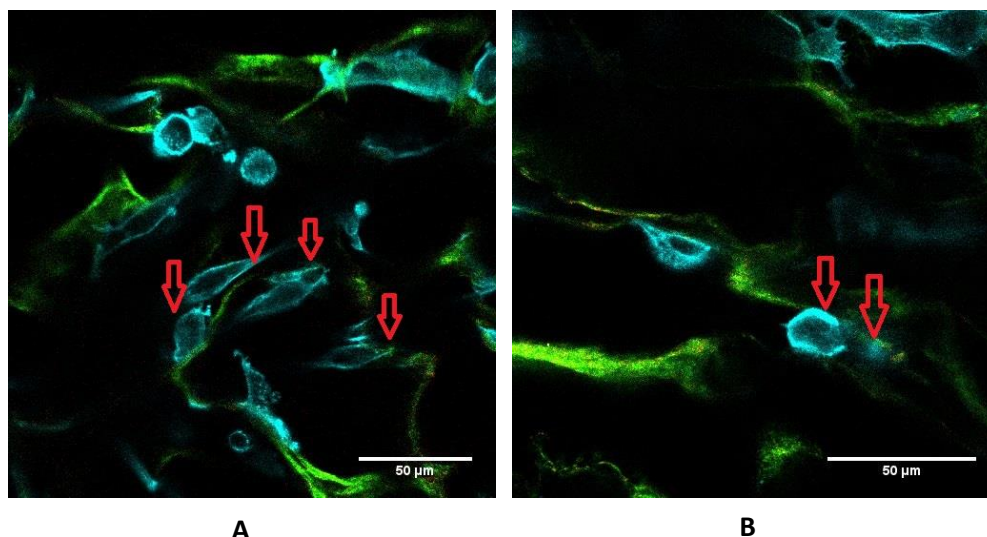


Figure 31: MDA-MB-231 cells in the scaffold developed at -55°C . **A)** The pore sizes match the maximum average polarized elongated-like cell diameter. This facilitates the cells in achieving elongated morphology. The red arrows mark the elongated cells. **B)** The cells form rounded cell morphology where the pore diameter is below $40\mu\text{m}$.

4.2.3.2 Porous ELP-RGD Scaffold

The two seeding techniques used for porous Collagen-HA constructs were tried on seeding porous ELP-RGD scaffolds. As with porous Collagen-HA scaffolds, the first seeding technique resulted in the cells settling beneath or around the porous scaffold. The cells were not able to attach to the boundaries of the pores. This prompted the use of the second cell seeding technique. As with porous Collagen-HA scaffolds, the porous ELP-RGD scaffolds had a gentle, turbid flow created through them with the cell seeding solution. Although, this seeding technique proved useful for the porous Collagen-HA scaffolds, it did not prove functional for seeding porous ELP-RGD scaffolds.

The porous ELP-RGD scaffolds have highly ordered pore morphology, and have a low standard deviation from mean pore size. The highly ordered patterning of the pores is not a representative of pores present *in vivo*. Furthermore, the failure of cell attachment into porous ELP-RGD scaffolds can be linked to the surface chemistry of the pores. From the ELP-RGD cell

encapsulation experiments, it was observed that the cells formed weak focal adhesions with ELP-RGD. Translating the thought onto the porous scaffolds elucidates the lack of cell attachment in the pores. Formation of weak focal adhesion sites on the pore boundaries could cause the cells to settle beneath the porous scaffolds.

4.2.3.3 Nanowrinkle ELP-RGD

Native ECM contains nanoscale physical topographies, and similar physical topographies on the engineered ECM could serve to better replicate *in vivo* behavior. Studies have established that nanoscale chemical and physical micro- and nano-topographies influence cell shape and morphology. There is also increasing evidence that micro- and nanotopographies influence cell migration [37]. With these studies in mind, the MDA-MB-231 cells were seeded onto 1D or oriented wrinkles and 2D or randomly oriented wrinkles. Three substrates were seeded; 1D having periodicity of 1.4 μ m and 3.7 μ m, 2D having periodicity of 4.5 μ m and a flat ELP-RGD substrate as control, see figure 32.

The cells seeded onto the flat surface adopted both rounded and elongated-like morphology. The flat surface represented a smooth surface with minimal surface topography. The lack of surface topography allowed the cells to orient themselves in random directions. On the other hand, the cells seeded on the 1D 1.6 μ m substrate, adopted the elongated-like morphology and oriented themselves parallel to the wrinkle direction, see figure 32. Similar phenomena were observed on the 1D 3.5 μ m. Furthermore, similar results have been reported with other cell lineages on wrinkled substrates[37]. Subsequent time-lapse studies on the 1D 1.6 μ m substrate showed that the cells migrate in parallel to the wrinkle direction. On the contrary, the cells seeded on the 2D 3.5 μ m wrinkles aligned themselves in randomly, with no specific orientation. This result was expected as the random orientation of the wrinkles did not provide a physical cue along which the cells could align.

The elongated morphology and alignment of cells on 1D substrates is concurrent with existing studies, where other cell types were seeded onto nano-patterned substrates [37]–[39]. The alignment of cells along the wrinkles serves as an ideal model to study a specific mode of cell migration termed as; multicellular streaming. This migration mode involved individual migration of cells one after another along the same microtrack with help from a chemoattractant [7].

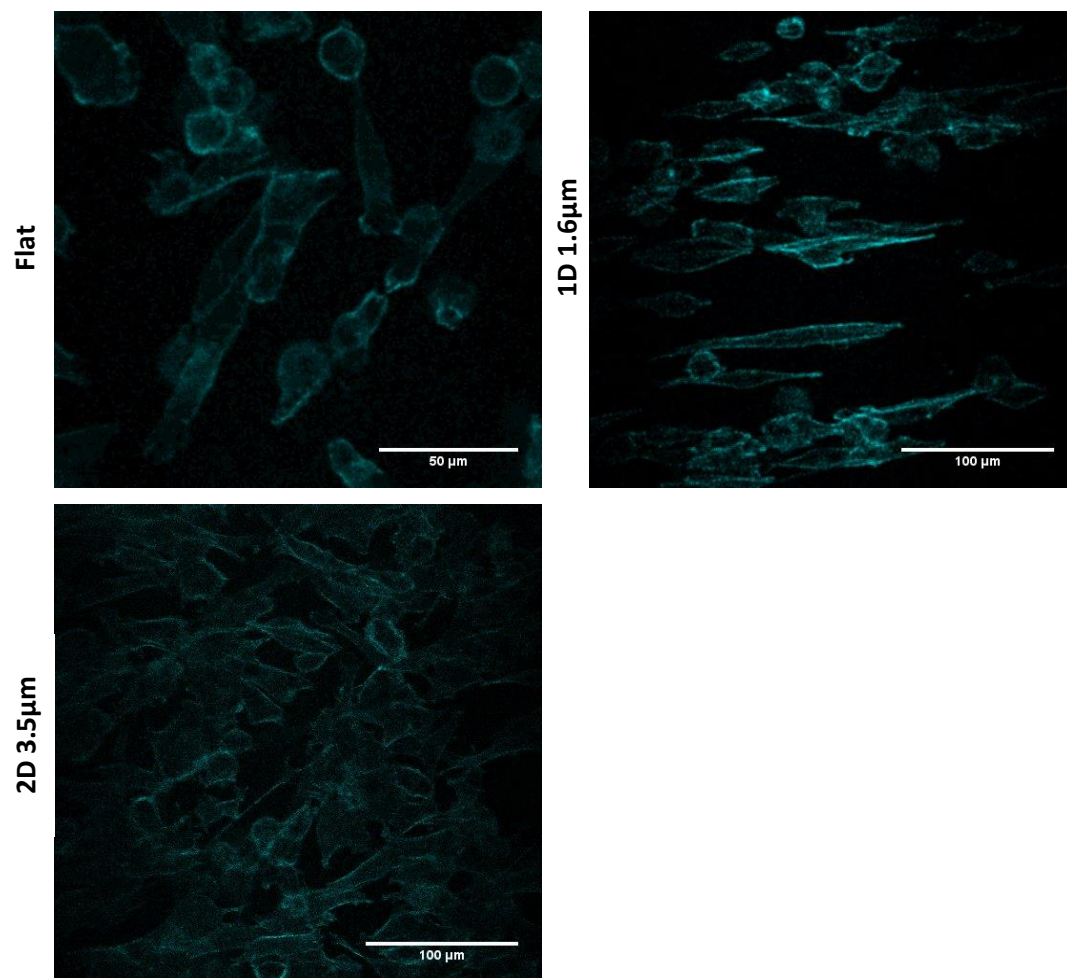


Figure 32: Actin stained images of MDA-MB-231 cells on flat, 1D 1.6 μm and 2D 3.5 μm ELP-RGD nanowrinkles samples. Random orientation of attachment is shown for cells on flat and 2D 3.5 μm while the cells align in parallel to the wrinkle on 1D 1.6 μm nanowrinkles.

4.2.3.4 Live-Cell Studies: Porous Collagen-HA and Nanowrinkle Scaffolds

A series of live-cell studies were performed on porous Collagen-HA and nanowrinkle scaffolds. The purpose of these studies was to observe the migration of cells within the constructs. No chemoattractants were incorporated in these studies.

4.2.3.4.1 Porous Collagen-HA Scaffolds

Live-cell studies were conducted on the -55°C scaffolds, 72 hours after seeding. The time delay allocated allowed sufficient time for the cells to adhere to the Collagen-HA boundaries. The study was conducted for a total of 10 hours, with images taken every 30 minutes. A set of two cells were targeted, which are marked with red circles within the field of view, see figure 33.

Both cells adhered to the boundary of the pores, and had rounded morphology. The change from rounded morphology to elongated morphology is evident as the time series progresses to 6 hours. After 8 hours it was noted that the cell had migrated inside the pore in the Z-direction. The close proximity of both cells after 10 hours suggests that cells may have made an attempt to ‘make contact’ with each other, with guidance from secreted chemoattractants.

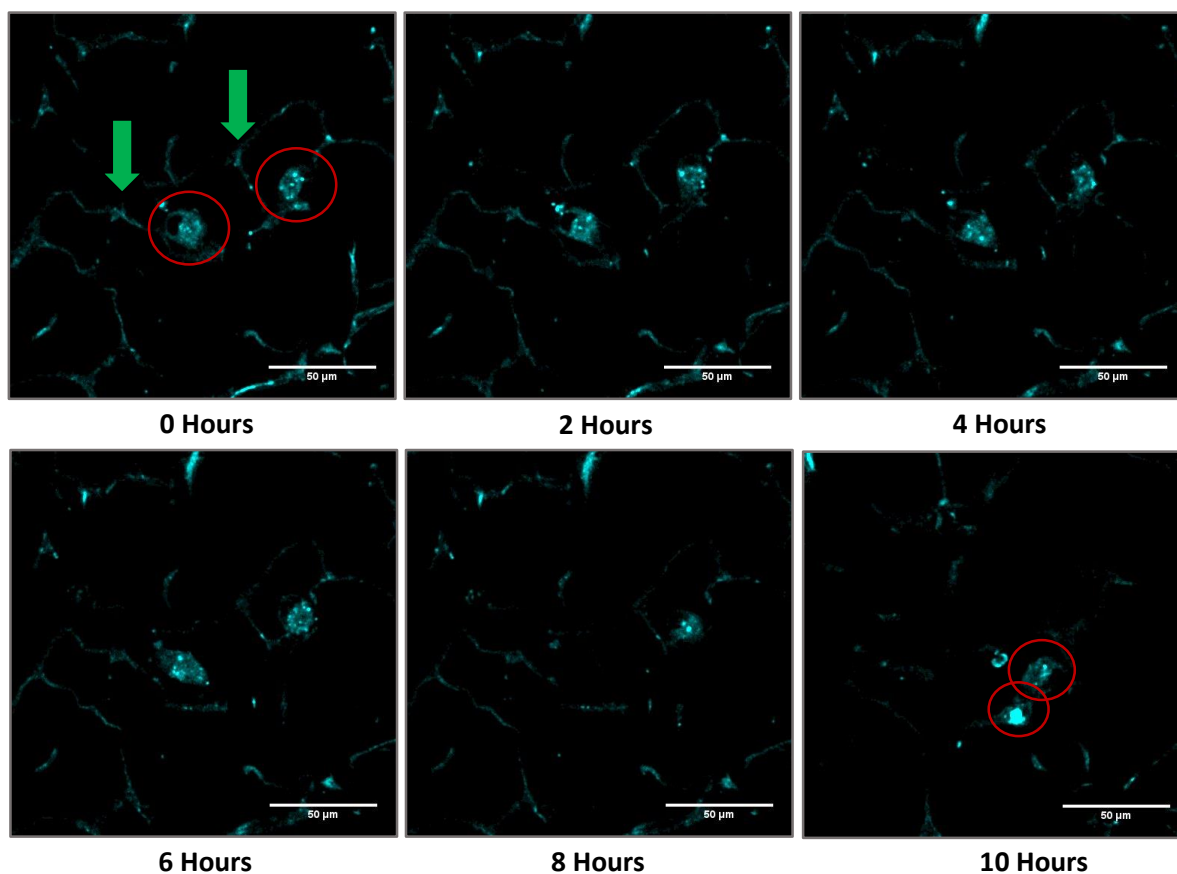


Figure 33: Time lapse of Cell Tracker Red stained MDA-MB-231 cells in porous Collagen-HA scaffolds developed at -55°C. Images were taken every 30 minutes for 10 hours. Images shown are every 2 hours after seeding. The red circles highlight the cells that were followed, while the green arrows point towards the col-HA boundary of the pores.

4.2.3.4.2 Nanowrinkle Scaffolds

Similar live-cell studies were performed on oriented 1D 1.4 μ m ELP-RGD and ELP-HA nanowrinkle scaffolds. It was speculated that the hybrid ELP-HA scaffold could induce cell migration in the invasive breast cancer cell line. HA concentrations are known to be higher at the tumor invasive front, and higher HA concentrations has been documented to increase the invasiveness of cancer cells [40].

As with the previous study, no external chemoattractants were incorporated. Live-imaging was performed 24 hours after seeding. For the ELP-RGD scaffold, the initial 10 hours of time lapse are shown, see figure 34. While, the ELP-HA was imaged for a total of 3 hours, with images taken every 30min, see figure 35.

For the ELP-RGD scaffold, a total of four cells were followed, which are marked by red circles in figure 34. The three cells within the field of view possessed an elongated morphology, indicating strong attachment to substrate. No significant movement was noticeable after 6 hours of live

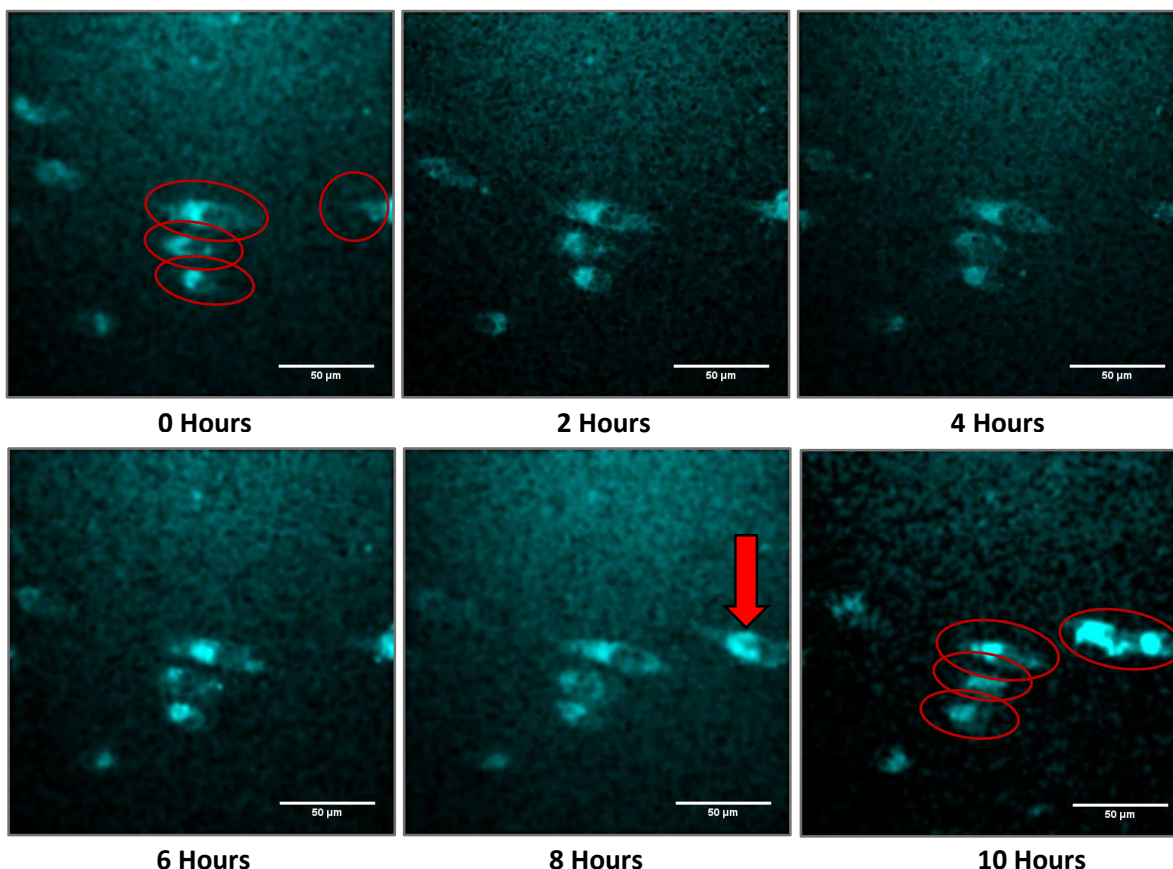


Figure 34: Time lapse of Cell Tracker Red stained MDA-MB-231 cells on ELP-RGD 1D 1.4 μ m nanowrinkle substrate. Images were taken every 30 minutes for 18 hours. Images shown are every 2 hours. The red circles highlight the cells that were followed.

imaging. However, the after 8 hours, a migrating cell is noticed, marked by a red arrow. This motile cell migrates into the field of view, and migrates alongside the nanowrinkle tracks; as

suggested by the orientation of the cells. The cell may have been possibly coaxed into migrating by secreted cellular chemoattractants.

A total of two cells were followed in the ELP-HA scaffold; marked in red circles in figure 35. The cells were followed for a total of 3 hours, images are shown every 30 minutes. Both cells possessed an elongated morphology, and were aligned uni-directionally, along the wrinkle orientation. Migration is observed in this duration with the cells adopting mesenchymal-like migration patterns [13].

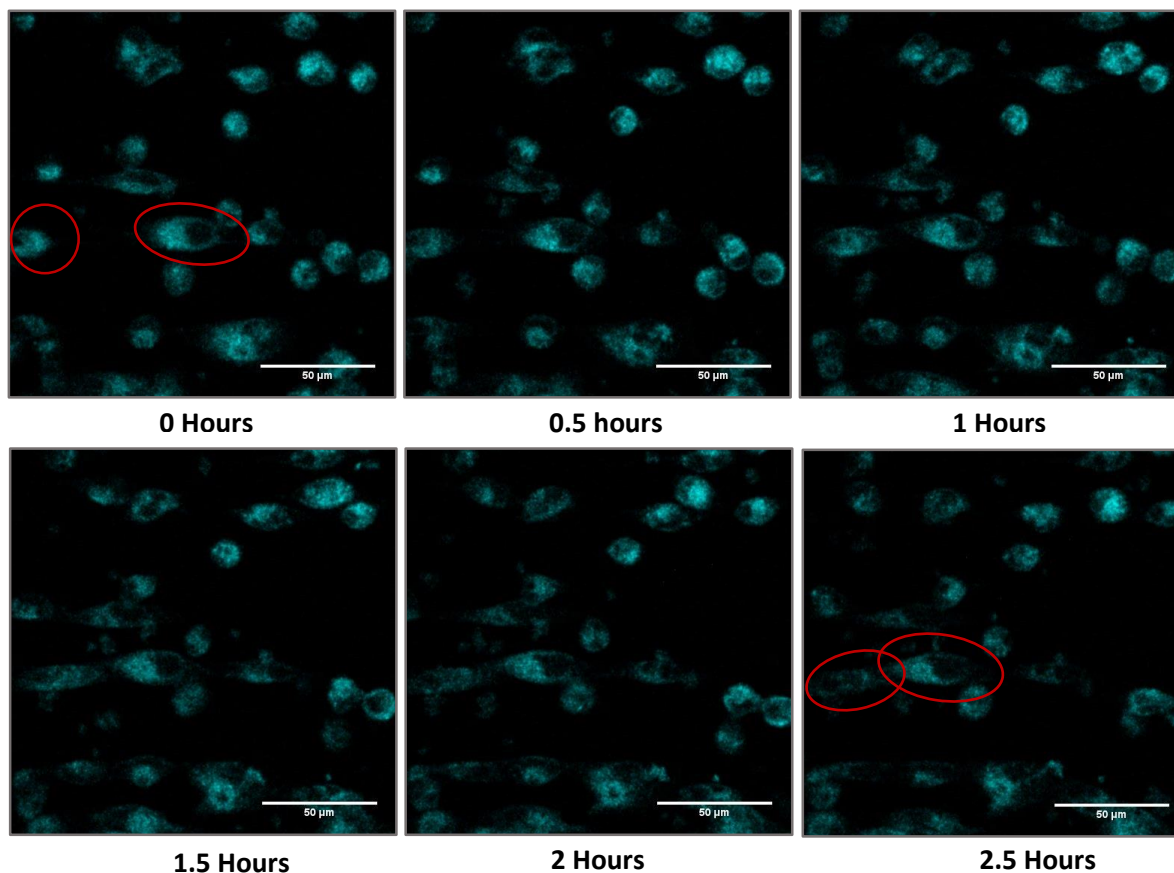


Figure 35: Time lapse of Cell Tracker Red stained MDA-MB-231 cells on ELP-HA 1D 1.4μm nanowrinkle substrate. Images were taken every 30 minutes for 3 hours. Images shown are every 30 minutes. The red circles highlight the cells that were followed.

Cells on both the ELP-RGD and ELP-HA scaffolds were observed to adopt mesenchymal-like migration patterns. Further, cells on both conditions migrated along wrinkle orientation; taking the wrinkle orientation as a micro-track. The latter reinforces the possibility of studying multicellular streaming on these scaffolds. The striking difference between the differing scaffolds was motility of the cells. Cells seeded onto ELP-HA scaffolds were observed to be greatly motile than the cells seeded on ELP-RGD scaffolds. The difference in motility between the two scaffolds can be associated to the invasive potential induced by HA [40].

5 Conclusion and Future Outlook

The metastatic site for epithelial breast cancer cells in the lung parenchyma consists of alveoli; which have Collagen type I and III pores that are highly interconnected. The developed porous collagen-HA and porous ELP-RGD scaffolds replicated this porous environment *in vitro*. The varying pore sizes and complexity of the scaffolds, not only mimicked *in vivo* alveoli but also influenced the morphology of the cells. It was noted that the cells adopted an elongated morphology for pore sizes ranging 40 μ m to 90 μ m. While, the cells preferred to adopt rounded morphology for pore sizes less than 40 μ m and greater than 90 μ m.

Additionally, the aligned ECM nature of the invasive tumor front was successfully replicated in *in vitro* by developing ELP-RGD and ELP-HA nanowrinkled scaffolds. The nanowrinkled scaffolds were shown to not only influence cell morphology, but also influence cell orientation and possibly influence cell migration patterns. A model to study a specific mode of cell migration termed, multi-cellular streaming, could be developed on the nanowrinkled scaffolds. This would require incorporation of a chemotactic gradient, and a study of the biological markers expressed by the cells.

It can be speculated that certain migrational modes would be preferred depending on the morphology of the cells. The migration of cells could be induced by incorporating a chemotactic gradient. Such studies would require additional investigation of in-depth time-lapse studies and a study of the biological markers expressed by the cells. In addition, the breast cancer cells can be co-cultured with lung cells on the developed scaffolds. Co-culturing would better simulate the cellular *in vivo* environment and an added dimension to study interaction between healthy and cancer cells could be studied.

6 Acknowledgements

I thank, both my supervisors, Alexandra Paul and Stéphanie Blockhuys for their supervision and patience throughout the duration of the project. My examiner, Annika Enejder. The MolMic group for their continued support and critique. And, my friends and family for their continued patience.

References

- [1] L. A. Torre, F. Bray, R. L. Siegel, J. Ferlay, J. Lortet-tieulent, and A. Jemal, “Global Cancer Statistics, 2012,” *CA a cancer J. Clin.*, vol. 65, no. 2, pp. 87–108, 2015.
- [2] J. Bin Kim, R. Stein, and M. O’Hare, “Three-dimensional in vitro tissue culture models of breast cancer - A review,” pp. 281–291, 2004.
- [3] D. Hanahan and R. A. Weinberg, “Hallmarks of cancer: The next generation,” *Cell*, vol. 144, no. 5, pp. 646–674, 2011.
- [4] T. Abraham and J. Hogg, “Extracellular matrix remodeling of lung alveolar walls in three dimensional space identified using second harmonic generation and multiphoton excitation fluorescence,” *J. Struct. Biol.*, vol. 171, no. 2, pp. 189–196, 2010.
- [5] K. Polyak and R. Kalluri, “The role of the microenvironment in mammary gland development and cancer,” *Cold Spring Harb. Perspect. Biol.*, vol. 2, no. 11, pp. 1–14, 2010.
- [6] B. Suki and J. H. T. Bates, “Extracellular matrix mechanics in lung parenchymal diseases,” *Respir. Physiol. Neurobiol.*, vol. 163, no. 1–3, pp. 33–43, 2008.
- [7] P. Friedl and S. Alexander, “Cancer invasion and the microenvironment: Plasticity and reciprocity,” *Cell*, vol. 147, no. 5, pp. 992–1009, 2011.
- [8] P. Friedl and K. Wolf, “Plasticity of cell migration: A multiscale tuning model,” *J. Cell Biol.*, vol. 188, no. 1, pp. 11–19, 2010.
- [9] A. G. Clark and D. M. Vignjevic, “Modes of cancer cell invasion and the role of the microenvironment,” *Curr. Opin. Cell Biol.*, vol. 36, pp. 13–22, 2015.
- [10] P. M. Vitorino, “Modular Control of Endothelial Sheet Cohesion and Collective Cell Migration,” *Stanford Univ. Thesis*, vol. 1, pp. 3268–3281, 2009.
- [11] R. Farooqui and G. Fenteany, “Multiple rows of cells behind an epithelial wound edge extend cryptic lamellipodia to collectively drive cell-sheet movement,” *J. Cell Sci.*, vol. 118, no. Pt 1, pp. 51–63, 2005.
- [12] B. a C. Harley, H.-D. Kim, M. H. Zaman, I. V Yannas, D. a Lauffenburger, and L. J. Gibson, “Microarchitecture of three-dimensional scaffolds influences cell migration behavior via junction interactions,” *Biophys. J.*, vol. 95, no. 8, pp. 4013–4024, 2008.
- [13] P. Friedl and K. Wolf, “Proteolytic interstitial cell migration: A five-step process,” *Cancer Metastasis Rev.*, vol. 28, no. 1–2, pp. 129–135, 2009.
- [14] C. L. Evans and X. S. Xie, “Coherent anti-stokes Raman scattering microscopy: chemical imaging for biology and medicine,” *Annu. Rev. Anal. Chem. (Palo Alto. Calif.)*, vol. 1, pp. 883–909, 2008.
- [15] M. Müller and A. Zumbusch, “Coherent anti-Stokes Raman scattering microscopy,” *ChemPhysChem*, vol. 8, no. 15, pp. 2157–2170, 2007.
- [16] J. F. McGilp, “A review of optical second-harmonic and sum-frequency generation at surfaces

- and interfaces,” *J. Phys. D. Appl. Phys.*, vol. 29, no. 7, pp. 1812–1821, 1999.
- [17] G. Cox and E. Kable, “Second-harmonic imaging of collagen,” *Methods Mol. Biol.*, vol. 319, no. 1, pp. 15–35, 2006.
 - [18] H. Wang, L. Cai, A. Paul, A. Enejder, and S. C. Heilshorn, “Hybrid Elastin-like Polypeptide-Polyethylene Glycol (ELP-PEG) Hydrogels with Improved Transparency and Independent Control of Matrix Mechanics and Cell Ligand Density,” *Biomacromolecules*, 2014.
 - [19] N. Annabi, J. W. Nichol, X. Zhong, C. Ji, S. Koshy, A. Khademhosseini, and F. Dehghani, “Controlling the porosity and microarchitecture of hydrogels for tissue engineering,” *Tissue Eng. Part B. Rev.*, vol. 16, no. 4, pp. 371–383, 2010.
 - [20] F. J. O’Brien, B. a. Harley, I. V. Yannas, and L. J. Gibson, “The effect of pore size on cell adhesion in collagen GAG scaffolds,” *Anat. Artic.*, vol. 1, no. 2, 2005.
 - [21] F. Khayyatan, S. Nemati, S. Kiani, S. H. Emami, and H. Baharvand, “Behaviour of human induced pluripotent stem cell-derived neural progenitors on collagen scaffolds varied in freezing temperature and laminin concentration,” *Cell J.*, vol. 16, no. 1, pp. 53–62, 2014.
 - [22] S. N. Park, J. C. Park, H. O. Kim, M. J. Song, and H. Suh, “Characterization of porous collagen/hyaluronic acid scaffold modified by 1-ethyl-3-(3-dimethylaminopropyl)carbodiimide cross-linking,” *Biomaterials*, vol. 23, no. 4, pp. 1205–1212, 2002.
 - [23] Y. Liu, L. Ma, and C. Gao, “Facile fabrication of the glutaraldehyde cross-linked collagen/chitosan porous scaffold for skin tissue engineering,” *Mater. Sci. Eng. C*, vol. 32, no. 8, pp. 2361–2366, 2012.
 - [24] M. Hanthamrongwit, M. H. Grant, and R. Wilkinson, “Confocal laser scanning microscopy (CLSM) for the study of collagen sponge microstructure,” *J. Biomed. Mater. Res.*, vol. 28, no. 2, pp. 213–216, 1994.
 - [25] L. Bi, Z. Cao, Y. Hu, Y. Song, L. Yu, B. Yang, J. Mu, Z. Huang, and Y. Han, “Effects of different cross-linking conditions on the properties of genipin-cross-linked chitosan/collagen scaffolds for cartilage tissue engineering,” *J. Mater. Sci. Mater. Med.*, vol. 22, no. 1, pp. 51–62, 2011.
 - [26] C. S. Ko, C. H. Wu, H. H. Huang, and I. M. Chu, “Genipin cross-linking of type II collagen-chondroitin sulfate-hyaluronan scaffold for articular cartilage therapy,” *J. Med. Biol. Eng.*, vol. 27, no. 1, pp. 7–14, 2007.
 - [27] U. Kim, C.-W. Shu, K. Y. Dane, P. S. Daugherty, J. Y. J. Wang, and H. T. Soh, “Selection of mammalian cells based on their cell-cycle phase using dielectrophoresis,” *Proc. Natl. Acad. Sci. U. S. A.*, vol. 104, no. 52, pp. 20708–12, 2007.
 - [28] Q. L. Loh and C. Choong, “Three-dimensional scaffolds for tissue engineering applications: role of porosity and pore size,” *Tissue Eng. Part B. Rev.*, vol. 19, no. 6, pp. 485–502, 2013.
 - [29] B. R. Williams, R. A. Gelman, D. C. Poppke, and K. A. Piez, “Collagen fibril formation. Optimal in vitro conditions and preliminar kinetic results,” *J. Biol. Chem.*, vol. 235, no. 18, pp. 6578–6585, 1978.

- [30] F. J. O'Brien, B. A. Harley, I. V. Yannas, and L. J. Gibson, "The effect of pore size on cell adhesion in collagen-GAG scaffolds," *Biomaterials*, vol. 26, no. 4, pp. 433–441, 2005.
- [31] H. W. Kang, Y. Tabata, and Y. Ikada, "Fabrication of porous gelatin scaffolds for tissue engineering," *Biomaterials*, vol. 20, no. 14, pp. 1339–1344, 1999.
- [32] L. B. Rocha, G. Goissis, and M. A. Rossi, "Biocompatibility of anionic collagen matrix as scaffold for bone healing," *Biomaterials*, vol. 23, no. 2, pp. 449–456, 2002.
- [33] I. V. Yannas, J. F. Burke, P. L. Gordon, C. Huang, and R. H. Rubenstein, "Design of an artificial skin. II. Control of chemical composition," *J. Biomed. Mater. Res.*, vol. 14, no. 2, pp. 107–132, 1980.
- [34] I. V. Yannas, E. Lee, D. P. Orgill, E. M. Skrabut, and G. F. Murphy, "Synthesis and characterization of a model extracellular matrix that induces partial regeneration of adult mammalian skin," *Proc. Natl. Acad. Sci. U. S. A.*, vol. 86, no. 3, pp. 933–937, 1989.
- [35] G. Maity, P. R. Choudhury, T. Sen, K. K. Ganguly, H. Sil, and A. Chatterjee, "Culture of human breast cancer cell line (MDA-MB-231) on fibronectin-coated surface induces pro-matrix metalloproteinase-9 expression and activity," *Tumor Biol.*, vol. 32, no. 1, pp. 129–138, 2011.
- [36] U. Hersel, C. Dahmen, and H. Kessler, "RGD modified polymers: Biomaterials for stimulated cell adhesion and beyond," *Biomaterials*, vol. 24, no. 24, pp. 4385–4415, 2003.
- [37] C. S. Ranucci and P. V. Moghe, "Substrate microtopography can enhance cell adhesive and migratory responsiveness to matrix ligand density," *J. Biomed. Mater. Res.*, vol. 54, no. 2, pp. 149–161, 2001.
- [38] D. H. Kim, P. P. Provenzano, C. L. Smith, and A. Levchenko, "Matrix nanotopography as a regulator of cell function," *J. Cell Biol.*, vol. 197, no. 3, pp. 351–360, 2012.
- [39] I. a. Janson and A. J. Putnam, "Extracellular matrix elasticity and topography: Material-based cues that affect cell function via conserved mechanisms," *J. Biomed. Mater. Res. - Part A*, pp. 1246–1258, 2014.
- [40] L. Udabage, G. R. Brownlee, S. K. Nilsson, and T. J. Brown, "The over-expression of HAS2, Hyal-2 and CD44 is implicated in the invasiveness of breast cancer," *Exp. Cell Res.*, vol. 310, no. 1, pp. 205–217, 2005.
- [41] P. T. C. So, "Two-photon Fluorescence Light Microscopy," *Life Sci.*, pp. 1–5, 2002.